

UC San Diego

UC San Diego Electronic Theses and Dissertations

Title

Restoration and Enhancement of Images Degraded by Light Scattering and Absorption

Permalink

<https://escholarship.org/uc/item/4n69n3qk>

Author

Peng, Yan-Tsung

Publication Date

2017

Peer reviewed|Thesis/dissertation

UNIVERSITY OF CALIFORNIA, SAN DIEGO

Restoration and Enhancement of Images Degraded by Light Scattering and Absorption

A dissertation submitted in partial satisfaction of the
requirements for the degree
Doctor of Philosophy

in

Electrical Engineering (Signal and Image Processing)

by

Yan-Tsung Peng

Committee in charge:

Professor Pamela Cosman, Chair
Professor William Hodgkiss
Professor Truong Nguyen
Professor Mohan Trivedi
Professor Geoff Voelker

2017

Copyright
Yan-Tsung Peng, 2017
All rights reserved.

The dissertation of Yan-Tsung Peng is approved, and it is acceptable in quality and form for publication on microfilm and electronically:

Chair

University of California, San Diego

2017

DEDICATION

To my family and my parents.

TABLE OF CONTENTS

Signature Page	iii
Dedication	iv
Table of Contents	v
List of Figures	vii
List of Tables	ix
Acknowledgements	x
Vita	xi
Abstract of the Dissertation	xii
Chapter 1	Introduction	1
	1.1 Image Formation Model	2
	1.2 Quality Assessment	5
	1.3 Thesis Structure	6
Chapter 2	Related Work	7
	2.1 Image Restoration using the IFM	7
	2.2 Underwater Transmission Estimation for the Red, Green, and Blue Channels	11
	2.3 DCP/MIP Exceptions caused by Artificial Illumination	13
	2.4 Acknowledgement	15
Chapter 3	Underwater Image Restoration	16
	3.1 Underwater Image Restoration based on Blurriness	16
	3.1.1 Experimental Results	18
	3.2 Image Restoration based on Blurriness and Light Absorption	19
	3.2.1 Ambient Light Estimation	20
	3.2.2 Depth Estimation based on Light Absorption and Image Blurriness	24
	3.2.3 Transmission Estimation and Scene Radiance Recovery	26
	3.2.4 Experimental Results	29
	3.2.4.1 Qualitative Assessment	29
	3.2.4.2 Quantitative Assessment	34
	3.2.4.3 Combining IFM-based Restoration and His- togram Equalization	40
	3.3 Acknowledgement	44

Chapter 4	Generalization of the Dark Channel Prior	47
	4.1 Ambient Light Estimation	48
	4.2 Scene Transmission Estimation	52
	4.3 DCP Generalization based on Scene Ambient Light Differential and depth-dependent color change	54
	4.3.1 Scene Radiance Restoration with Adaptive Color Correction	57
	4.4 Experimental Results	59
	4.4.1 Qualitative Assessment	60
	4.4.2 Quantitative Assessment	64
	4.5 Acknowledgement	65
Chapter 5	Conclusion and Future Work	69
Bibliography	71

LIST OF FIGURES

Figure 1.1:	(a)–(e) Examples of different images degraded by light scattering and absorption. (f) IFM.	2
Figure 2.1:	The flowchart of DCP-based image restoration.	10
Figure 2.2:	Examples of depth estimation via the DCP (I_{dcp}^{rgb}) for sandstorm and underwater images.	11
Figure 2.3:	An example of inaccurate transmission and ambient light estimation causing an unsatisfying restoration result.	13
Figure 2.4:	An example of restoring an underwater image with artificial lighting using [16] and the proposed method in Section 3.2.	15
Figure 3.1:	An example of image blurriness estimation. (a) Original image, (b) Initial blurriness map from Eq. (3.1), (c) Rough map from Eq. (3.2), (d) Refined map from Eq. (3.3).	17
Figure 3.2:	Examples of underwater image enhancement in different lighting conditions.	19
Figure 3.3:	The flowchart of our proposed UIBLAR method. The original image is from [59].	20
Figure 3.4:	Examples of changing brightness or hue of restored scene radiance via varying ambient light with given transmission maps obtained using our UIBLAR method.	22
Figure 3.5:	An example of ambient light estimation using Algo. 1.	24
Figure 3.6:	Examples of depth estimation based on light absorption and image blurriness.	27
Figure 3.7:	An example of transmission estimation with and without \tilde{d}_0	29
Figure 3.8:	A restoration example where all methods are successful.	30
Figure 3.9:	An example of restoring an underwater image with dim ambient light.	30
Figure 3.10:	An example of restoring a greenish underwater image.	31
Figure 3.11:	An example of restoring an underwater image with artificial lighting.	31
Figure 3.12:	A close comparison between (a) the UIBR method (Section 3.1) and (b) the UIBLAR method (Section 3.2) for the original image shown in Fig. 3.11.	32
Figure 3.13:	A restoration example involving artificial lighting.	33
Figure 3.14:	Examples of synthesizing underwater images with four different underwater color tones using Eq. (3.16). (a) The ground truth image and its depth map. (b)–(e) Synthesized underwater images with $d_0 = 4$ and $r_s = 4$	35
Figure 3.15:	All test synthesized underwater images with Tone I color.	36
Figure 3.16:	PSNR results (top) and SSIM results (bottom) obtained using different restoration methods for “TestMode–InitD.”	39

Figure 3.17: PSNR results (top) and SSIM results (bottom) obtained using different methods for “TestMode–ScaleD.”	40
Figure 3.18: Examples of restoring synthesized underwater images with Tone I–IV colors in “TestMode–ScaleD” ($r_s = 3$) obtained using the UIBLAR method.	41
Figure 3.19: Examples of synthesized underwater images generated using three different images with their depth maps and selected ambient lights.	42
Figure 3.20: Examples of “BRISQUE score/UIQM value” pairs for synthesized (top) and real (bottom) underwater images. (The images are from [53, 59, 68], and Google Images.)	42
Figure 3.21: Test images for BRISQUE. (The images are from [1, 12, 16, 19, 34, 59, 68], and Google Images.)	43
Figure 3.22: Comparisons between the processed images obtained using [1] and the UIBLAR method with and without contrast enhancement.	46
Figure 4.1: The flowchart of our GDCP method. The original image is from [11].	48
Figure 4.2: The flowchart of the depth-dependent color change determination.	50
Figure 4.3: The significance weighting function.	51
Figure 4.4: Comparisons of depth estimation based on the DCP [7, 10–14], DCP variants [15, 16, 39], and the GDCP method for images with different light lighting conditions and color casts.	53
Figure 4.5: Examples of changing hue or brightness of restored scene radiance by adjusting ambient light with given transmission estimated using the GDCP method.	58
Figure 4.6: Examples of scene radiance restoration with and without adaptive color correction.	60
Figure 4.7: A restoration example where all methods are successful.	61
Figure 4.8: An example of restoring a dark hazy image with a color cast.	61
Figure 4.9: Restoring the dark hazy image with a color cast in Fig. 4.8	62
Figure 4.10: Example of restoring sandstorm images with different color distributions.	64
Figure 4.11: Example of restoring an underwater images with different color tones and lighting conditions.	67
Figure 4.12: Terrestrial images for quantitative testing. The images are from [6, 7, 10, 11], and Google Images.	68
Figure 4.13: Underwater images for quantitative testing. The images are from [16, 19, 59], and Google Images.	68

LIST OF TABLES

Table 2.1:	Adopted priors, ambient light estimation, and transmission estimation for various image restoration methods [12, 14–17, 19, 34, 39]	12
Table 2.2:	Formulas of different priors [7, 15, 16, 19, 38, 39]	12
Table 3.1:	Comparison of average PSNR/SSIM of the restoration results over all the tested $d_0 \in [4, 8 m]$ and $r_s \in [1, 5]$ obtained using the UIBLAR method and its mixed methods using the TM estimation for the red channel \tilde{t}^r based on DCPs, MIP, or image blurriness.	43
Table 3.2:	Comparison of average PSNR/SSIM of the restoration results over all the tested $d_0 \in [4, 8 m]$ for “TestMode–InitD.”	44
Table 3.3:	Comparison of average PSNR/SSIM of the restoration results over all the tested $r_s \in [1, 5]$ for “TestMode–ScaleD.”	44
Table 3.4:	Comparison of average PSNR/SSIM of the restoration results over all the tested d_0 for “TestMode–InitD.”	45
Table 3.5:	Comparison of average PSNR/SSIM of the restoration results over all the tested r_s for “TestMode–ScaleD.”	45
Table 3.6:	Comparison of average PSNR/SSIM of the restoration results over all the tested d_0 and r_s obtained using the UIBLAR method and its mixed methods using the TM estimation for the red channel \tilde{t}^r based on DCPs, MIP, or image blurriness.	45
Table 3.7:	Average BRISQUE scores and UIQM values of the original images in Fig. 3.21 and their restored versions from all the compared methods.	45
Table 4.1:	Average e , \bar{r} and NIQE values for the restored images from all the compared methods of Fig. 4.12.	65
Table 4.2:	Average UIQM, UCIQE, and NIQE values of the original images in Fig. 4.13 and their restored versions from all the compared methods.	66

ACKNOWLEDGEMENTS

First of all, I would like to thank Professor Pamela Cosman for being my advisor. Professor Cosman has provided me with a lot of freedom and support for my research, always inspiring me to think and delve deeper into the essence of research topics with her shrewd guidance and valuable suggestions.

Chapter 2, in part is a reprint of a published paper, Y.-T. Peng and P. C. Cosman, “Underwater Image Restoration based on Image Blurriness and Light Absorption,” *IEEE Trans. Image Process.*, vol. 26, no. 4, pp. 1579-1594, Apr. 2017, and of a submitted paper, Y.-T. Peng, K. Cao, and P. C. Cosman, “Generalization of the Dark Channel Prior for Single Image Restoration” (submitted to *IEEE Trans. Image Process.*, Jul. 2017). The dissertation author was the primary investigator and author of these papers.

Chapter 3, in full, is a reprint of two published papers, Y.-T. Peng and P. C. Cosman, “Underwater Image Restoration based on Image Blurriness and Light Absorption,” *IEEE Trans. Image Process.*, vol. 26, no. 4, pp. 1579-1594, Apr. 2017, and Y.-T. Peng, X. Zhao and P.C. Cosman, “Single Underwater Image Enhancement using Depth Estimation based on Blurriness,” *IEEE Int. Conf. on Imag. Process. (ICIP)*, pp. 4952-4956, Sep. 2015. The dissertation author was the primary investigator and author of these papers.

Chapter 4, in full, is a reprint of a published paper, Y.-T. Peng and P. C. Cosman, “Single Image Restoration using Scene Ambient Light Differential,” *IEEE Int. Conf. on Imag. Process. (ICIP)*, pp. 1953-1957, Sep. 2016, and of a submitted paper, Y.-T. Peng, K. Cao, and P. C. Cosman, “Generalization of the Dark Channel Prior for Single Image Restoration” (submitted to *IEEE Trans. Image Process.*, Jul. 2017). The dissertation author was the primary investigator and author of these papers.

VITA

- 2002 B. S. in Computer Science and Engineering, Yuan Ze University, Taiwan
- 2004 M. S. in Computer Science and Information Engineering, National Chiao Tung University, Taiwan
- 2017 Ph. D. in Electrical Engineering (Signal and Image Processing), University of California, San Diego, USA

PUBLICATIONS

- K. Cao, **Y.-T. Peng**, P. C. Cosman, “Underwater Image Restoration using Deep Networks to Estimate Background Light and Scene Depth.” (submitted to *IEEE SSIAI*, 2018)
- Y.-T. Peng**, K. Cao, and P. C. Cosman, “Generalization of the Dark Channel Prior for Single Image Restoration.” (submitted to *IEEE Trans. Image Process.*, Jul. 2017)
- Y.-T. Peng** and P. C. Cosman, “Underwater Image Restoration based on Image Blurriness and Light Absorption,” *IEEE Trans. Image Process.*, vol. 26, no. 4, pp. 1579-1594, Apr. 2017.
- Y.-T. Peng** and P. C. Cosman, “Single Image Restoration using Scene Ambient Light Differential,” *IEEE Int. Conf. on Imag. Process. (ICIP)*, pp. 1953-1957, Sep. 2016.
- Y.-T. Peng**, X. Zhao and P.C. Cosman, “Single Underwater Image Enhancement using Depth Estimation based on Blurriness,” *IEEE Int. Conf. on Imag. Process. (ICIP)*, pp. 4952-4956, Sep. 2015. (one of the **top 10%** papers).
- Y.-T. Peng** and P. C. Cosman “Weighted boundary matching error concealment for HEVC using block partition decisions,” *48th Asilomar Conf. on Signals, Syst. and Comput.*, pp. 921-925, Nov. 2014.

ABSTRACT OF THE DISSERTATION

Restoration and Enhancement of Images Degraded by Light Scattering and Absorption

by

Yan-Tsung Peng

Doctor of Philosophy in Electrical Engineering (Signal and Image Processing)

University of California, San Diego, 2017

Professor Pamela Cosman, Chair

Images degraded by light scattering and absorption such as hazy, sandstorm, and underwater images often suffer from color distortion and low contrast because of light traveling through turbid media. This can prevent systems that operate outdoors in different lighting conditions from functioning properly, for example, video surveillance systems, autopilot systems and intelligent transportation systems, which include automatic license plate recognition, automatic traffic counting, etc. Therefore, it is desirable to develop an effective method to restore color and enhance contrast for these images. This thesis presents novel work to advance research on image restoration and enhancement for such

images.

To enhance or restore such a degraded image, the image formation model is often used to describe it as a “clear” image blended with an ambient light based on the scene transmission computed using the scene depth from the camera. The transmission describes the portion of the scene radiance which is not scattered or absorbed and which reaches the camera. By reversing the image formation process, one can attain the scene radiance from a degraded image, which is a “clear” image. However, it involves solving an ill-posed and under-constrained problem because we need to estimate both the ambient light and scene transmission from a single degraded image.

To attack this problem, we proposed to use image blurriness to estimate ambient light and scene depth for underwater images. Furthermore, we extended it by combining light absorption and blurriness to estimate scene depth for underwater scenes in different lighting conditions and color tones. For any images degraded by light scattering and absorption, not limited to underwater ones, we proposed a generalization of the common dark channel prior approach for ambient light and transmission estimation. Additionally, adaptive color correction is incorporated into the image formation model for removing color casts while restoring contrast. Based on the experimental results, our proposed algorithms outperform, both subjectively and objectively, other state-of-the-art algorithms based on the image formation model.

Chapter 1

Introduction

Images or videos captured in different conditions sometimes suffer from visibility degradation because light is scattered and absorbed with distance from the camera through turbid media, such as fog, haze, sandstorms, or water. The degradation reduces the visual quality of the images and videos and affects the performance of computer vision applications. Thus, developing an effective method to restore color and contrast for such images is desirable.

Even though there are many image enhancement techniques developed, such as white balance, color correction, histogram equalization, and fusion-based methods [1, 2], they are not based on a physical model, and thus are not applicable for images degraded by light scattering and absorption with different physical properties. It is challenging to restore such images because of the variation of physical properties of different transmission media. For example, light attenuation underwater leads to different degrees of color change, depending on wavelength, dissolved organic compounds, water salinity, and concentration of phytoplankton [3]. In water, red light with a longer wavelength is absorbed more than green and blue light. In a sandstorm, blue light is absorbed by sand. Fig. 1.1(a)-(e) shows five different images degraded by light scattering

and absorption. Also, scattered ambient light coming from different colors of media is blended with the scene radiance along the line of sight, resulting in underwater scenes often having low contrast and color distortions.

1.1 Image Formation Model

Images captured when light travels through turbid media, such as fog, sand, and water, etc. are degraded by light scattering and absorption. Although the media are different, their underlying physical influences on imaging are similar [4, 5], meaning that such images can be described by the image formation model (IFM). Fig. 1.1(f) shows how an image is described using the IFM [4–6]. The image formation equation is given by:

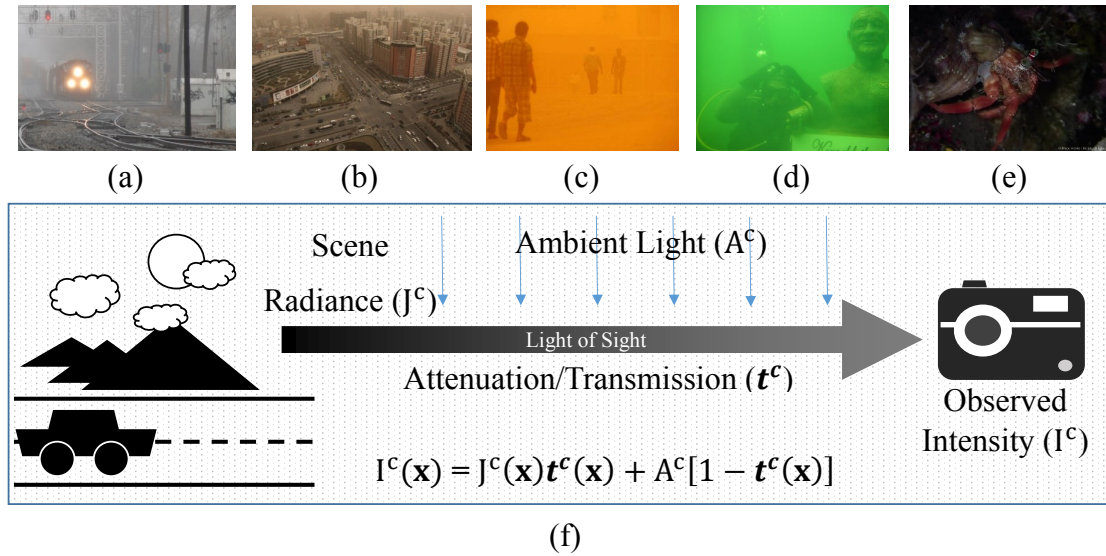


Figure 1.1: (a)–(e) Examples of different images degraded by light scattering and absorption. (f) IFM. The original image (a) is from [7], (b) is from [10], (c) is from [58] (d) is from [1] and (e) is from [59].

$$I^c(\mathbf{x}) = J^c(\mathbf{x})t^c(\mathbf{x}) + A^c(1 - t^c(\mathbf{x})), c \in \{r, g, b\}, \quad (1.1)$$

where \mathbf{x} is a 2×1 vector that depicts the coordinates of a pixel in an image, $I^c(\mathbf{x})$ is the observed intensity of the pixel, $J^c(\mathbf{x})$ is the scene radiance, A^c is the ambient light, and t^c is the transmission map, where c is one of the red, green, and blue channels. The observed intensity I^c , which is a degraded image, consists of the scene radiance J^c blended with the ambient light A^c according to the transmission maps t^c , where transmission describes the portion of the scene radiance which is not scattered or absorbed and which reaches the camera. Thus, a larger value in the transmission map means that the corresponding scene point is closer to the camera. Note that I^c , J^c , and A^c are assumed to be in a range $[0, 1]$.

In order to restore images degraded by light scattering and absorption, there has been much research [7–11] on image defogging and visibility restoration using the IFM [6]. Using the IFM, He et al. [7] proposed the dark channel prior (DCP) to remove fog/haze in natural terrestrial images via estimation of the ambient light and transmission. It was observed that because points in the scene closer to the camera have a shorter path over which scattering occurs, close dark scene points would remain dark as they would experience less brightening from scattered light. Thus, the DCP can be used to estimate transmission and scene depth. The ambient light can be estimated from the farthest scene points based on the scene depth. This motivated many image restoration approaches [8–19] that improve and extend the DCP for different goals and applications. However, haze with different color casts may lead to under- or over-estimated transmission based on the DCP, causing poor restoration results. A color cast is defined as a tint of a particular color, often unwanted [20]. In [10, 11], restoration methods for hazy and sandstorm images were presented; they used adaptive gamma correction to solve the transmission over-estimation caused by the low observed intensity due to color casts, and adopted color correction to compensate for the color cast. Nevertheless, the underlying reason for inaccurate transmission estimation for images with color casts

is that the DCP is not as reliable for such images as for those without color casts. This problem often cannot be solved only by gamma correction. Hence, these methods are unable to restore heavily tinted sandstorm images because most blue light is scattered and absorbed, which causes the DCP to fail and leads to inaccurate ambient light and transmission estimation. In order to estimate medium transmission more precisely, some researchers exploited learning algorithms to generate a mapping function where the input is a hazy image, and the output is its depth map [21–23]. However, these methods that train their mapping functions using synthetic hazy images with bright ambient light are often unable to restore hazy images with color casts.

Several studies also have been conducted on restoring underwater images based on the DCP [12–14, 17, 18] or its variants [15, 16]. However, measuring transmission for underwater images based on the DCP [12–14, 17] frequently fails to generate accurate results since red light is more attenuated than other wavelengths underwater, and thus the DCP based on RGB channels ends up considering only the red channel, causing unreliable transmission estimation. Several DCP variants consider only the green and blue channels [15], the RGB channels with the red inverted [16], or the minimal information loss principle (MILP) [18] to try to estimate transmission underwater, but they may still fail due to different underwater lighting conditions and color tones. Instead of using the DCP, the maximum intensity prior (MIP) approach [19] calculates the difference between the maximum intensity of the red channel and that of the green and blue channels to estimate transmission. However, these methods frequently perform poorly as the light absorption and lighting conditions that exist in underwater images invalidate these priors. For example, all the DCP-, MIP-, and MILP-based restoration methods are unable to restore underwater images with dim ambient light, where the background pixels are dark and would be wrongly judged as being close.

1.2 Quality Assessment

One can use no-reference quality assessment tools or full-reference approaches in order to objectively evaluate image restoration methods. No-reference image quality assessment approaches measure image quality using only the input image itself. There are general no-reference image quality metrics that use natural scene statistics to quantify possible losses of “naturalness” for the input image, such as Blind/Referenceless Image Spatial QUality Evaluator (BRISQUE) [24] and Natural Image Quality Evaluator (NIQE) [25]. Some no-reference image quality metrics are designed for specific types of images, such as Contrast Enhancement Metric (CEM) [26] for ocean scenes in fog, Underwater Image Quality Measure (UIQM) [27], and Underwater Color Image Quality Evaluation Metric (UCIQE) [28]. CEM uses human observations and low-level contrast enhancement metrics to measure image quality for foggy scenes. UIQM is a linear combination of three underwater image attribute measures: the colorfulness (UICM), sharpness (UISM), and contrast (UIConM) measures, where $UIQM = c_1 \times UICM + c_2 \times UISM + c_3 \times UIConM$. UCIQE quantifies image quality via a linear combination of the variation of chrominance, average saturation, and luminance contrast. A greater value for both the UIQM and UCIQE all represent higher image quality.

Full-reference image quality assessment approaches require both the input image and the reference image for quality evaluation. For example, PSNR and SSIM [29] are full-reference image metrics measuring reconstruction quality and similarity. PSNR is defined via the mean squared error (MSE) between the input and reference images. The SSIM index is a similarity measure that consists of three comparison measurements between the input and reference images: luminance, contrast, and structure. Additionally, there are two full-reference contrast metrics that measure gradient ratios at visible edges [30], where one is the metric e that calculates an edge restoration rate and the other

is the metric r that assesses quality of contrast restoration.

1.3 Thesis Structure

In this thesis, we propose to effectively restore and enhance images degraded by light scattering and absorption, such as hazy, sandstorm and underwater images. The rest of the thesis is organized as follows. In Chapter 2, current research on image restoration using the IFM is reviewed and discussed. Chapter 3 describes our underwater image restoration method based on image blurriness and light absorption. In Chapter 4, a generalization of the Dark Channel Prior is proposed to estimate ambient light and scene transmission for images degraded by light scattering and absorption. Chapter 5 summarizes the conclusions and discusses directions for future work.

Chapter 2

Related Work

In this chapter, previous work on restoration and enhancement for images degraded by light scattering and absorption using the IFM will be discussed. First, the DCP-based method [7] is reviewed, which basically consists of two parts: 1) ambient estimation and 2) transmission estimation. Next, several variants of ambient light and transmission estimation methods will be summarized.

2.1 Image Restoration using the IFM

Assuming that light attenuation is homogeneous, the IFM is $I^c(\mathbf{x}) = J^c(\mathbf{x})t^c(\mathbf{x}) + A^c(1 - t^c(\mathbf{x}))$, $c \in \{r, g, b\}$, where the transmission t^c can be written as an exponential decay term [7, 16, 17] based on the Beer-Lambert law [31] of light attenuation:

$$t^c(\mathbf{x}) = e^{-\beta^c d(\mathbf{x})}, \quad (2.1)$$

where $d(\mathbf{x})$ is the distance from the camera to the radiant object and β^c is the spectral volume attenuation coefficient for channel c , where c is one of the red, green, and blue channels. For hazy terrestrial images, there are three general assumptions: overcast light-

ing, spatially invariant attenuation coefficients, and wavelength-independent attenuation $\beta^r = \beta^g = \beta^b = \beta$, *i.e.*, $t^r = t^g = t^b = t$ [5]. Therefore, the IFM under these assumptions is $I^c(\mathbf{x}) = J^c(\mathbf{x})t(\mathbf{x}) + A^c(1 - t(\mathbf{x}))$, $c \in \{r, g, b\}$, as described in Eq. (1.1).

For hazy images, the DCP was proposed by He et al. [7] to estimation ambient light and transmission. For each pixel \mathbf{x} in an image, the DCP finds the minimum value among RGB channels in a local patch $\Omega(\mathbf{x})$ centered at \mathbf{x} , that is:

$$J_{dcp}^{rgb}(\mathbf{x}) = \min_{\mathbf{y} \in \Omega(\mathbf{x})} \left\{ \min_{c \in \{r, g, b\}} J^c(\mathbf{y}) \right\}. \quad (2.2)$$

For an outdoor terrestrial haze-free image, J_{dcp}^{rgb} is often close to zero, because at least one of the three color channels will typically have a low-intensity pixel in the local patch in $\Omega(\mathbf{x})$. It was asserted in [1, Eq. (9)] that $J_{dcp}^{rgb} = 0$ for about 75% of non-sky pixels in haze-free images.

Dividing both sides of Eq. (1.1) by A^c and applying the minimum operators to it, the term involving J^c is dropped as being close to zero, and the transmission estimate $\tilde{t}_{rgb}(\mathbf{x}) = \min_{\mathbf{y} \in \Omega(\mathbf{x})} t(\mathbf{y})$, described in [4, Eq. (11)], is

$$\tilde{t}_{rgb}(\mathbf{x}) = 1 - \min_{\mathbf{y} \in \Omega(\mathbf{x})} \left\{ \min_{c \in \{r, g, b\}} \frac{I^c(\mathbf{y})}{A^c} \right\}. \quad (2.3)$$

Since \tilde{t}_{rgb} has block-like artifacts, it can be refined by median filtering [9], image matting [32], or guided filtering [33]. To estimate A^c , the DCP for a hazy image is calculated as:

$$I_{dcp}^{rgb}(\mathbf{x}) = \min_{\mathbf{y} \in \Omega(\mathbf{x})} \left\{ \min_{c \in \{r, g, b\}} I^c(\mathbf{y}) \right\}. \quad (2.4)$$

For the DCP of a hazy image, a far and a close scene point, \mathbf{x}_f and \mathbf{x}_c , generally have a relation that $I_{dcp}^{rgb}(\mathbf{x}_c) \leq I_{dcp}^{rgb}(\mathbf{x}_f)$ because of scattered light through haze. Therefore, I_{dcp}^{rgb} can provide depth information for a hazy image I . Based on I_{dcp}^{rgb} , ambient light A^c is selected from one of the farthest and haziest pixels in the input image. In [7], the top

0.1% brightest pixels in I_{dcp}^{rgb} were picked. Let $P^{0.1\%}$ be the set of positions of those bright pixels in I_{dcp}^{rgb} . Then, among these pixels, the one with the highest intensity in the input image I^c is chosen to provide the estimate of ambient light. The estimated ambient light A^c can be described as:

$$A^c = I^c \left(\underset{\mathbf{x} \in P^{0.1\%}}{\mathbf{argmax}} \sum_{c \in \{r,g,b\}} I^c(\mathbf{x}) \right). \quad (2.5)$$

Finally, by putting I^c , \tilde{t} and A^c into Eq. (1.1), the estimated scene radiance is calculated as:

$$J^c(\mathbf{x}) = \frac{I^c(\mathbf{x}) - A^c}{\max(\tilde{t}^c(\mathbf{x}), t_0)} + A^c, \quad (2.6)$$

where t_0 is empirically set in the range $[0.1, 0.4]$ to increase the exposure of J^c for display. Note that for the following chapters, if only one transmission map is mentioned in an image restoration method, it means wavelength-independent attenuation is assumed, which is $t^r = t^g = t^b = t$. Fig. 2.1 shows the flowchart of DCP-based image restoration. As can be seen in Fig. 2.1(e), the restored scene radiance with haze removed has better contrast.

As previously stated, this method works under three general assumptions. Therefore, if this method is applied to restoring images degraded by light scattering and absorption with different lighting conditions and color casts, such as sandstorm, underwater or dimly-lit images, it only works in limited cases. Such images have different possible lighting conditions and color casts, which may violate the assumptions underlying the DCP, leading to inaccurate ambient light and transmission estimation and producing poor restoration results. Fig. 2.2 gives two successful and two failure examples of depth estimation using the DCP (I_{dcp}^{rgb}). The lighting conditions for the original images in the first two columns of Fig. 2.2 are appropriate to the DCP-based methods. As can be seen, their foreground has dark pixels which cause the dark channel to have a small value, so

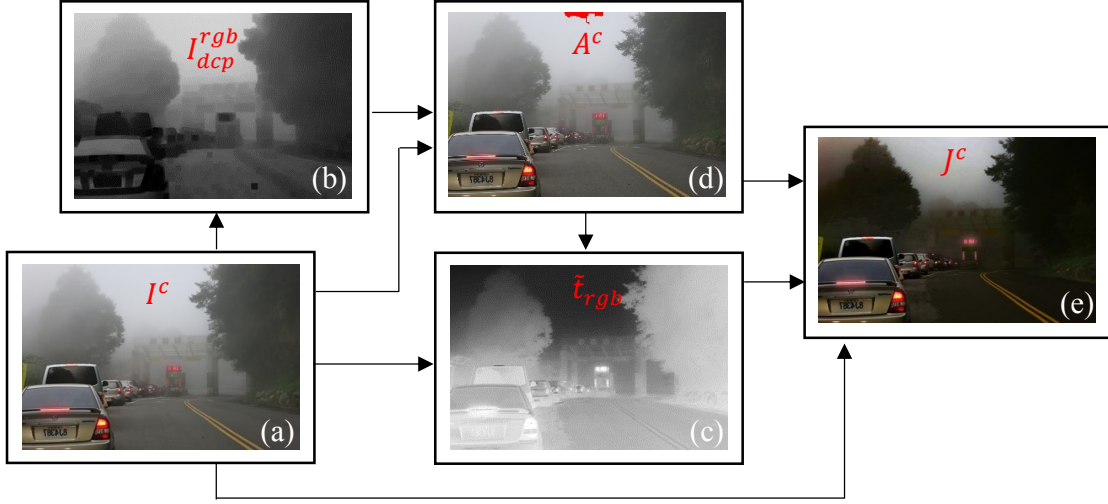


Figure 2.1: The flowchart of DCP-based image restoration. (a) Original hazy image I^c . (b) DCP of the hazy image I_{dcp}^{rgb} , Eq. (2.4). (c) Estimated transmission \tilde{t}_{rgb} , Eq. (2.3). (d) Ambient light pixels (marked in red), Eq. (2.5). (e) Restored scene radiance J^c , Eq. (2.6).

they are correctly estimated as being close, while their background looks hazy and lacks dark pixels, so these regions are correctly estimated to be relatively far away.

By contrast, the original images in the last two columns of Fig. 2.2 are examples where the DCP works poorly. The sandstorm image in the third column of Fig. 2.2 has very small values in the blue channel, so the DCP in Eq. (2.4) has small values everywhere, which come from the blue channel, and the entire scene is mistakenly judged as being very close. The underwater image in the fourth column was captured with artificial lights. In this case, the bright foreground is erroneously viewed as being far while the dark background is incorrectly deemed to be close.

In order to extend the DCP for different light scattering and absorption conditions, several DCP variants were proposed for ambient light and transmission estimation with different lighting conditions and color casts [12, 14–17, 19, 34] or dimly-lit images [39]. Table 2.1 lists various priors, and ambient and transmission estimation methods for different restoration methods based on Eq. (2.6). Table 2.2 gives detailed formulas for








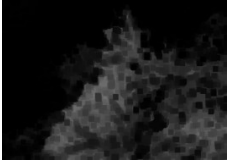
	Success		Failure	
I				
I_{dcp}				
	(a)	(b)	(c)	(d)

Figure 2.2: Examples of depth estimation via the DCP (I_{dcp}^{rgb}) for sandstorm and underwater images. (a) and (b) are successful cases while (c) and (d) are failure cases. The original images of (a), (b), (c) and (d) come from [7], [59], [58], and [19].

those priors.

2.2 Underwater Transmission Estimation for the Red, Green, and Blue Channels

Image restoration methods that rely on the three assumptions for the IFM often fail to recover scene radiance underwater because imaging conditions are quite different from those in open air. The natural illumination underwater undergoes a strong color-dependent attenuation, which violates the assumption of wavelength-independent attenuation $\beta^r = \beta^g = \beta^b$.

Chiang et al. [14] first addressed this problem by proposing a wavelength compensation and image dehazing method for underwater scenes. In this, scene transmission is estimated according to residual energy ratios of different color channels, related to the attenuation coefficients β^c . However, these ratios were chosen manually, limiting the practical applicability of this method.

Table 2.1: Adopted priors, ambient light estimation, and transmission estimation for various image restoration methods [12, 14–17, 19, 34, 39]

Method	Prior (p) on I^c	Ambient light estimation (A^c)	Transmission estimation (\tilde{t} or \tilde{t}^r)
[12]	I_{dcp}^{rgb}	$I^c(\mathbf{argmax}_{\mathbf{x}} p(\mathbf{x}))$	$\tilde{t}_{rgb}(\mathbf{x}) = 1 - \min_{c,y \in \Omega(\mathbf{x})} \{I^c(\mathbf{y})A^c\}$
[19]	D_{mip}	$I^c(\mathbf{argmin}_{\mathbf{x}} \tilde{t}(\mathbf{x}))$	$\tilde{t}_{D_{mip}}(\mathbf{x}) = D_{mip}(\mathbf{x}) + (1 - \max_{\mathbf{x}} D_{mip}(\mathbf{x}))$
[14]	I_{dcp}^{rgb}	$I^c(\mathbf{argmax}_{\mathbf{x}} I_{dcp}^c(\mathbf{x}))$	$\tilde{t}^r(\mathbf{x}) = 1 - \min_{c,y \in \Omega(\mathbf{x})} \left\{ \frac{I^c(\mathbf{y})}{A^k} \right\}, \tilde{t}^{c'} = (\tilde{t}^r)^{\frac{\beta^{c'}}{\beta^r}}$
[34]	I_{dcp}^{gb}	$I^c\left(\mathbf{argmin}_{\mathbf{x}} \left(I_{dcp}^r(\mathbf{x}) - \max_{c'} (I_{dcp}^{c'}(\mathbf{x})) \right)\right)$	$\tilde{t}^g(\mathbf{x}) = \tilde{t}^b(\mathbf{x}) = 1 - \min_{c',y \in \Omega(\mathbf{x})} \left\{ \frac{I^c(\mathbf{y})}{A^{c'}} \right\},$ $\tilde{t}^r = (\tau \max_{y \in \Omega(\mathbf{x})} I^r(\mathbf{y})), \tau = \frac{\mathbf{avg}_{\mathbf{x}}(\tilde{t}^r(\mathbf{x}))}{\mathbf{avg}_{\mathbf{x}}(\max_{y \in \Omega(\mathbf{x})} I^r(\mathbf{y}))}$
[15]	I_{dcp}^{gb}	$I^c(\mathbf{argmax}_{\mathbf{x}} p(\mathbf{x}))$	$\tilde{t}_{gb}(\mathbf{x}) = 1 - \min_{c',y \in \Omega(\mathbf{x})} \left\{ \frac{I^c(\mathbf{y})}{A^{c'}} \right\}$
[16]	$I_{dcp}^{r'gb}$	$I^c(\mathbf{argmin}_{\mathbf{x} \in p_{0.1\%,c'}^{10\%,c'}} I^r(\mathbf{x}))$	$\tilde{t}_{r'gb}(\mathbf{x}) = 1 - \min_{y \in \Omega(\mathbf{x})} \left\{ \frac{1-I^r(\mathbf{y})}{1-A^r}, \frac{I^g(\mathbf{y})}{A^g}, \frac{I^b(\mathbf{y})}{A^b} \right\}$
[17]	I_{dcp}^{rgb}	$I^c\left(\mathbf{argmax}_{\mathbf{x} \in p_{0.1\%,c'}} I^r(\mathbf{x}) - I^{c'}(\mathbf{x}) \right)$	$\tilde{t}^r(\mathbf{x}) = 1 - \min_{c,y \in \Omega(\mathbf{x})} \left\{ \frac{I^c(\mathbf{y})}{A^c} \right\}, \tilde{t}^{c'} = (\tilde{t}^r)^{\frac{\beta^{c'}}{\beta^r}}$
[39]	$I_{dcp}^{r'g'b'}$	$I^c(\mathbf{argmin}_{\mathbf{x} \in p_{0.1\%,c'}^{0.1\%,c'}} (\sum_k I^k(\mathbf{x})))$	$\tilde{t}_{r'g'b'}(\mathbf{x}) = 1 - \min_{c,y \in \Omega(\mathbf{x})} \left\{ \frac{1-I^c(\mathbf{y})}{1-A^c} \right\}$

$$c \in \{r, g, b\}; c' \in \{g, b\};$$

Table 2.2: Formulas of different priors [7, 15, 16, 19, 38, 39]

Method	Prior on I^c	Formula
[7]	$I_{dcp}^{rgb}(\mathbf{x})$	$\min_{c \in \{r, g, b\}, y \in \Omega(\mathbf{x})} \{I^c(\mathbf{y})\}$
[19]	$D_{mip}(\mathbf{x})$	$\max_{y \in \Omega(\mathbf{x})} I^r(\mathbf{y}) - \max_{c \in \{g, b\}, y \in \Omega(\mathbf{x})} \{I^c(\mathbf{y})\}$
[15]	$I_{dcp}^{gb}(\mathbf{x})$	$\min_{c \in \{g, b\}, y \in \Omega(\mathbf{x})} \{I^c(\mathbf{y})\}$
[16]	$I_{dcp}^{r'gb}(\mathbf{x})$	$\min_{y \in \Omega(\mathbf{x})} \{1 - I^r(\mathbf{y}), I^g(\mathbf{y}), I^b(\mathbf{y})\}$
[38, 39]	$I_{dcp}^{r'g'b'}(\mathbf{x})$	$\min_{c \in \{r, g, b\}, y \in \Omega(\mathbf{x})} \{1 - I^c(\mathbf{y})\}$

In [17], the relations among the attenuation coefficients of different color channels based on inherent optical properties of water were derived from the ambient light as:

$$\frac{\beta^k}{\beta^r} = \frac{A^r(m\lambda^k + i)}{A^k(m\lambda^r + i)}, k \in \{g, b\}, \quad (2.7)$$

where $\lambda^c, c \in \{r, g, b\}$, represent the wavelengths of the red, green, and blue channels, $m = -0.00113$, and $i = 1.62517$. The transmission maps for the green and blue lights are then calculated by:

$$t^k(\mathbf{x}) = t^r(\mathbf{x})^{\frac{\beta^k}{\beta^r}}, k \in \{g, b\}, \quad (2.8)$$

where t^r is estimated by Eq. (2.3).

As described above, transmission estimation is contingent on the prior and ambient light it uses. Both of these frequently cannot be attained in [14, 17] because the prior they use is the I_{dcp}^{rgb} . Fig. 2.3 shows an example of a poor restoration result produced using incorrect ambient light and transmission estimation based on I_{dcp}^{rgb} in [17]. Here, the original image has some bright foreground pixels and some dark background pixels. Thus, instead of picking ambient light from the bright background pixels, the method selects ambient light from foreground pixels erroneously regarded as being far. Moreover, wrong ambient light causes transmission maps for RGB channels, \tilde{t}^r , \tilde{t}^g , and \tilde{t}^b , to be similar to each other for this greenish input image, thus failing to correct the distorted color.

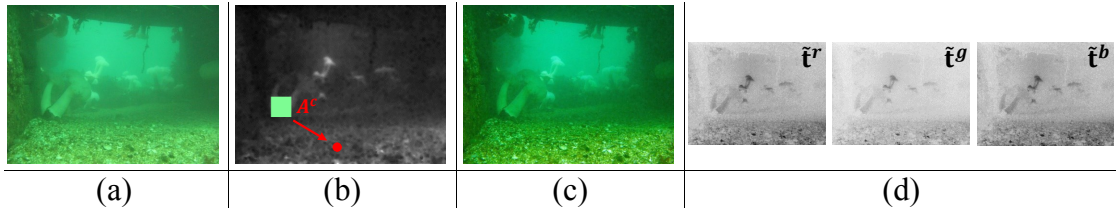


Figure 2.3: An example of inaccurate transmission and ambient light estimation causing an unsatisfying restoration result. (a) Original image, (b) depth map, and estimated ambient light A^c picked at the position of the red dot, (c) recovered scene radiance obtained using [17], and (d) estimated transmission maps for the red, green, and blue channels.

2.3 DCP/MIP Exceptions caused by Artificial Illumination

Since water absorbs more light as the light rays travel through longer distance in the water, artificial lighting is sometimes used to provide sufficient light for taking pictures and videos. Artificial lighting in an underwater image often leads to a bright foreground. This violates the assumptions underlying the DCP, where bright pixels are

regarded as being far. Artificially illuminated bright foreground pixels should be less modified by a restoration method than background pixels because the light, originating from an artificial lighting source and reflected by foreground objects, travels less far in the water and is less absorbed and scattered. Depth estimation based on the MIP could fail when the foreground has bright pixels and the background has dark pixels because the values of D_{mip} for the foreground and the background would be similar, which is unable to produce an accurate depth map. Examples will be demonstrated and discussed more in Chapter. 3.

Chiang et al. [14] proposed to detect and then remove artificial lighting by comparing the mean luminances of the foreground and the background. However, this approach classifies foreground and background pixels based on the depth map using the DCP, which is often ineffective because of incorrect depth estimation.

Galdran et al. [16] dealt with artificial lighting by incorporating the saturation prior into $I'_{dcp}{}^{r'gb}$ as:

$$I'_{dcp}{}^{r'gb-sat}(\mathbf{x}) = \min_{y \in \Omega(\mathbf{x})} \left\{ \min_{c \in \{r', g, b\}} I^c(y), Sat(y) \right\}, \quad (2.9)$$

where $Sat = \frac{\max_c(I^c) - \min_c(I^c)}{\max_c(I^c)}$, $c \in \{r, g, b\}$ measures the saturation of scene point y . Because it is assumed that artificially illuminated scene points would have low saturation, these bright points in the foreground would not be incorrectly judged as being far. However, it does not solve the problem caused by dark pixels in the background, which still violate the assumptions underlying the DCP. As shown in Fig. 2.4(b), restoration based on $I'_{dcp}{}^{r'gb}$ estimates the scene depth incorrectly, as the rock in the foreground has bright pixels because of artificial lighting, so is wrongly judged to be far. In Fig. 2.4(c), depth estimation based on the $I'_{dcp}{}^{r'gb}$ with saturation successfully avoids this problem, but the dark pixels in the background are still erroneously estimated to be close, also resulting in

an incorrect ambient light selection and poor restoration result. With more accurately estimated transmission and properly selected ambient light, Fig. 2.4(d) shows a better restoration result image.

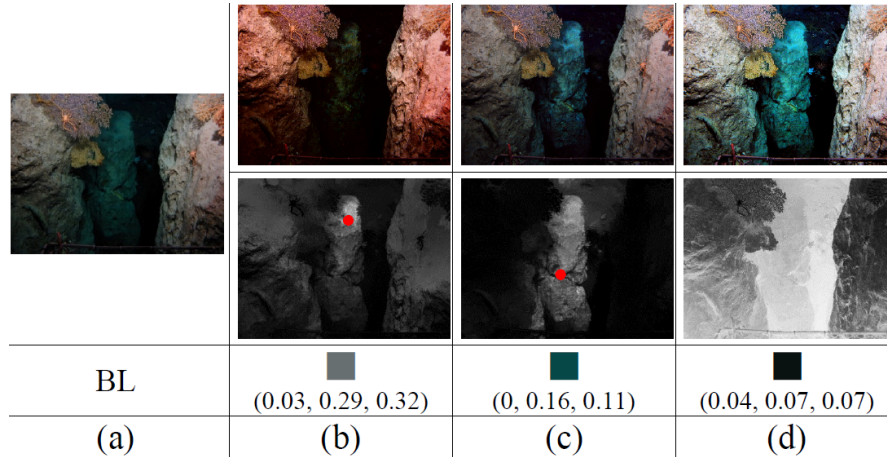


Figure 2.4: An example of restoring an underwater image with artificial lighting using [16] and the proposed method in Section 3.2. (a) The original image. The restoration results and their corresponding depth maps and ambient light (marked with a red dot) obtained using (b) [16] based on the $I'_{dcp}{}^{rgb}$, (c) [16] based on the $I'_{dcp}{}^{rgb}$ with saturation, and (d) a more accurate depth map and properly selected ambient light. The original image is from [59].

2.4 Acknowledgement

This chapter, in part is a reprint of a published paper, Y.-T. Peng and P. C. Cosman, “Underwater Image Restoration based on Image Blurriness and Light Absorption,” *IEEE Trans. Image Process.*, vol. 26, no. 4, pp. 1579-1594, Apr. 2017, and of a submitted paper, Y.-T. Peng, K. Cao, and P. C. Cosman, “Generalization of the Dark Channel Prior for Single Image Restoration” (submitted to *IEEE Trans. Image Process.*, Jul. 2017). The dissertation author was the primary investigator and author of these papers.

Chapter 3

Underwater Image Restoration

In this chapter, image blurriness is estimated and applied to restoring underwater images, which is based on the observation that objects farther from the camera are more blurry for underwater images. There are two restoration methods introduced. One is based on image blurriness only, and the other uses both image blurriness and light absorption.

3.1 Underwater Image Restoration based on Blurriness

In this section, our Underwater Image Blurriness-based restoration method (UIBR) is proposed. Underwater image blurriness estimation includes three steps. Let $G^{k,\sigma}$ be the input image filtered by a $k \times k$ spatial Gaussian filter with variance σ^2 . The initial blurriness map P_{init} is computed as:

$$P_{init}(\mathbf{x}) = \frac{1}{n} \sum_{i=1}^n |I_g(\mathbf{x}) - G^{k,\sigma}(\mathbf{x})|, \quad (3.1)$$

where I_g is the grayscale version of the input image I^c . Both k and σ are set to $2^i n + 1$, and n is set to 4. Next, we apply the max filter to calculate the rough blurriness map P_r .

as:

$$P_r(\mathbf{x}) = \max_{\mathbf{y} \in \Omega(\mathbf{x})} P_{init}(\mathbf{y}), \quad (3.2)$$

where $\Omega(\mathbf{x})$ is a $z \times z$ local patch centered at \mathbf{x} . Here, we set $z = 7$. (We found that any patch size from $z = 7$ up to $z = 31$ works well for image sizes ranging from 800x600 to 1280x720 in the proposed method of Section 3.2. So $z = 7$ is used throughout this chapter.) We refine P_r by filling the holes caused by flat regions in the objects using morphological reconstruction [42], and then soft matting [32] or guided filtering [33] is applied for smoothing to generate a refined blurriness map P_{blr} :

$$P_{blr}(\mathbf{x}) = F_g \left\{ C_r [P_r(\mathbf{x})] \right\}, \quad (3.3)$$

where C_r is a hole-filling morphological reconstruction operator, and F_g is the soft matting or guided filtering function. Fig. 3.1 shows an example of each step.

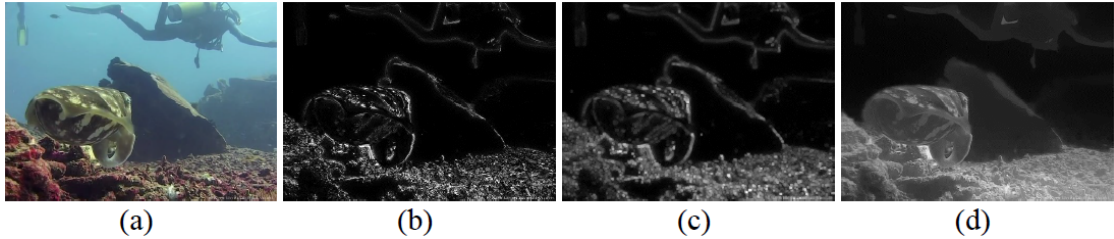


Figure 3.1: An example of image blurriness estimation. (a) Original image, (b) Initial blurriness map from Eq. (3.1), (c) Rough map from Eq. (3.2), (d) Refined map from Eq. (3.3).

The blurriness map P_{blr} can be regarded as an inverted scene depth map, where larger values represent close scene points, and small values represent farther scene points. Therefore it can be used to estimate the transmission map directly by stretching it to a proper range $[r_0, r_1]$ as:

$$\tilde{t}(\mathbf{x}) = \frac{[P_{blr}(\mathbf{x}) - \min(P_{blr})](r_1 - r_0)}{\max(P_{blr}) - \min(P_{blr})} + r_0. \quad (3.4)$$

Ambient light is estimated using the 0.1% farthest scene points based on P_{blr} , which means that we choose those pixels in the input image with the bottom 0.1% smallest values in P_{blr} to estimate ambient light using Eq. (2.5). Finally, we recover the scene radiance J using Eq. (2.6) with the estimated ambient light and \tilde{t} calculated in Eq. (3.4).

3.1.1 Experimental Results

Previous methods for underwater image restoration only used DCP- or MIP-based methods. In this section, we compare our UIBR against the DCP- and MIP-based methods. The performance of our method is evaluated by visual comparison with other methods as well as the examination of the transmission map. We use four underwater images captured in different lighting conditions for testing, shown in Fig. 3.2, where the transmission maps all undergo simple individual contrast stretching or scaling steps for display here.

In Ex.1 of Fig. 3.2, all of the result images look properly enhanced even though they have a little color difference. Although the transmission map and ambient light are both inaccurately estimated by [13], its enhanced result is good only because of extra color correction process in [13].

In Ex.2, the imprecise transmission maps generated by [19], [13], and [34] cause color distortion in the output images while our method presents more natural color and better contrast.

In Ex.3, color distortion can be found in the output images obtained by [13] and [34] due to erroneous transmission estimation while the result images yielded by [19] and ours are enhanced with better global contrast.

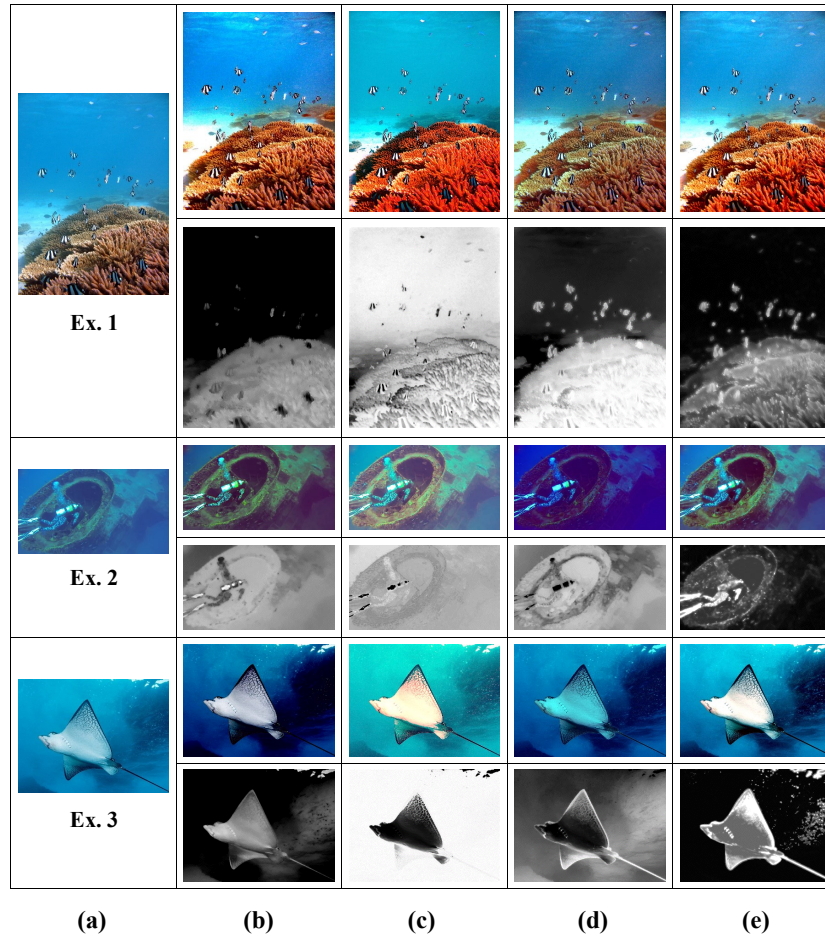


Figure 3.2: Examples of underwater image enhancement in different lighting conditions. (a) Original image. The enhanced images and the corresponding depth maps obtained using (b) [19], (c) [13], (d) [34], and (e) the proposed UIBR method.

3.2 Image Restoration based on Blurriness and Light Absorption

In this section, our Image-Blurriness-and-Light-Absorption Restoration method (UIBLAR) is proposed, which generates more accurate ambient light and depth estimation. First, we select the ambient light from blurry regions in an underwater image. Then, based on the ambient light, the depth map and the transmission maps are obtained to

restore scene radiance. The flowchart of this method is shown in Fig. 3.3.

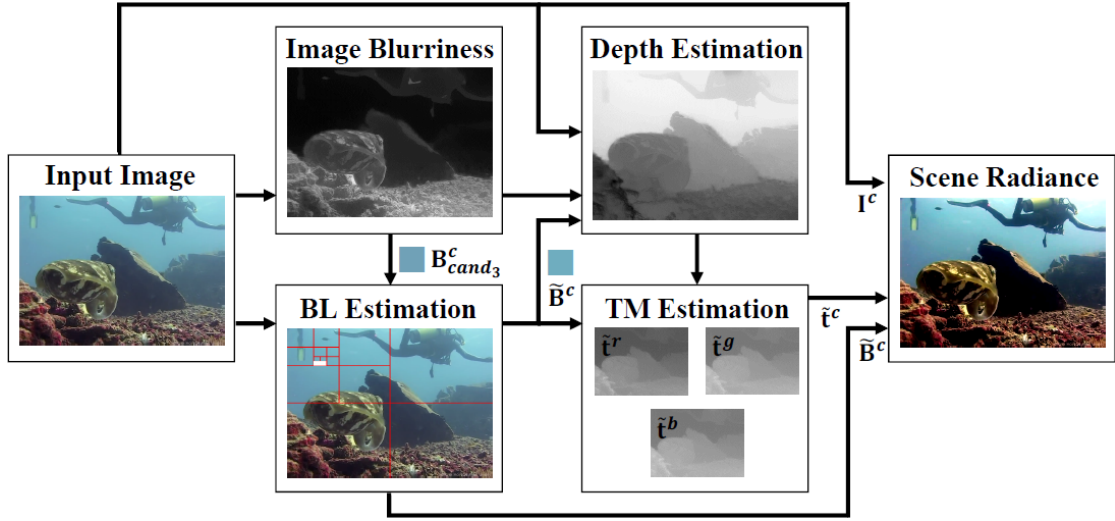


Figure 3.3: The flowchart of our proposed UIBLAR method. The original image is from [59].

3.2.1 Ambient Light Estimation

Ambient light determines the color tone of an underwater image as well as its restored scene radiance. For an underwater image, the lower and upper bounds of its possible restored scene radiance $J^c \in [0, 1]$ can be derived by setting $A^c = 1$ and $A^c = 0$ in Eq. (2.6), as:

$$\max\left(\frac{I^c - 1 + \tilde{t}^c}{\tilde{t}^c}, 0\right) \leq J^c \leq \min\left(\frac{I^c}{\tilde{t}^c}, 1\right), \quad (3.5)$$

where $\tilde{t}^c = \max(\tilde{t}^c, t_0) \in [t_0, 1]$. Based on Eq. (3.5), restoring an underwater image with dim ambient light would result in bright scene radiance while using bright ambient light leads to an opposite result. Consider an extreme ambient light, $A^c = 0$, as an example, where $J^c = \min(\frac{I^c}{\tilde{t}^c}, 1)$. In this case, the restored scene radiance $J^c(\mathbf{x})$ of a far scene point with the value of $\tilde{t}^c(\mathbf{x})$ being small would have a larger value than its corresponding observed intensity $I^c(\mathbf{x})$ and thus be brighter. A bright ambient light would lead to the opposite result. A visual example can be seen in the first row of Fig. 3.4. As the ambient

light, though unchanging, is estimated as being brighter, the restored scene radiance gets darker. Moreover, a small value in one of the color channels of the estimated ambient light will lead to a substantial increase in that color in the restored image. The second row of Fig. 3.4 gives an example in which changing values in the red channel of A^c produces different hues of the restored images.

In general, the value for estimated ambient light of an underwater image is chosen from far scene points with high intensity. Emberton et al. [35] adopted a hierarchical rank-based approach based on I_{dcp}^{sb} , color variance, and gradient to find the brightest pixel in the most likely region of ambient light. This method is, however, inaccurate in many cases, as it still uses the assumptions of I_{dcp}^{sb} . In contrast, we estimate the ambient light based on image blurriness and variance. We propose an ambient light candidate selection method which picks three ambient light candidates from the top 0.1% blurry pixels in the input image, the lowest variance region and the largest blurriness region. These two regions (which may or may not be the same) are decided using quadtree decomposition which iteratively divides the input image into four equal-sized blocks according to the variance or blurriness. The blurriness of a region in the input image is obtained by averaging $P_{blr}(\mathbf{x})$ in the corresponding region in the blurriness map.

With three ambient light candidates determined, we pick ambient light for each color channel separately from them according to the input image. The detailed algorithm is described in Algo. 1, where S is a sigmoid function given by:

$$S(a, v) = \left[1 + e^{-s(a-v)} \right]^{-1}, \quad (3.6)$$

where s is an empirical constant. Here, we set $s = 32$. The fixed thresholds we used are $\epsilon_s = 2^{-10}$ and $\epsilon_n = 0.2$. Note that the function QUAD-SELECT-LV is a similar function to QUAD-SELECT-LB with largest blurriness being replaced by lowest variance and without considering P_{blr} .

In AL-ESTIMATE, we determine ambient light for each color channel between the darkest and brightest ambient light candidates according to the percentage of bright pixels ($I^k > 0.5$). When the percentage is high ($\frac{|I^k > 0.5|}{\text{Size}(I^k)} \gg \epsilon_n$), meaning that the input image was taken under sufficient lighting, then ambient light estimated as being brighter is more suitable. When the image was taken without sufficient lighting ($\frac{|I^k > 0.5|}{\text{Size}(I^k)} \ll \epsilon_n$), ambient light is estimated as being darker. In between these extremes, the ambient light estimate is calculated by a weighted combination of the darkest and brightest ambient light candidates. Fig. 3.5 demonstrates the proposed ambient light estimation and compares the restoration results obtained using each ambient light candidate and the selected estimated ambient light, where we can see that using our ambient light candidate selection method generates a more visually pleasing result.

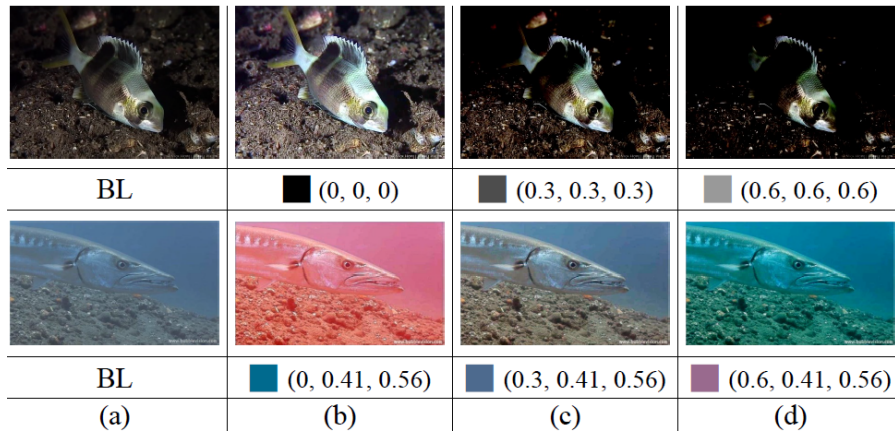


Figure 3.4: Examples of changing brightness or hue of restored scene radiance via varying ambient light with given transmission maps obtained using our UIBLAR method. (a) Original images. (b), (c), and (d) are the restored images using different ambient light. The original images are from [59].

Algorithm 1 AL-Estimate

```

1: Input parameter: input image  $I^c$ , blurriness map  $P_{blr}$ .
2: Output parameter: estimated ambient light  $A^c$ .
3:
4: function AL-ESTIMATE( $I^c, P_{blr}$ )
5:    $A_{cand_1}^c \leftarrow \mathbf{avg}_x [\text{QUAD-SELECT-LV}(I^c)];$ 
6:    $A_{cand_2}^c \leftarrow \mathbf{avg}_x [\text{QUAD-SELECT-LB}(I^c, P_{blr})];$ 
7:    $A_{cand_3}^c \leftarrow \frac{1}{|P_{0.1\%}|} \sum_{x \in P_{0.1\%}} I^c(\mathbf{x});$ 
8:    $A_{max}^c \leftarrow \max_{i \in \{1,2,3\}} A_{cand_i}^c;$ 
9:    $A_{min}^c \leftarrow \min_{i \in \{1,2,3\}} A_{cand_i}^c;$ 
10:  for  $k \in \{r, g, b\}$  do
11:     $\alpha \leftarrow S(\frac{|I^k|_{>0.5}}{\text{Size}(I^k)}, \epsilon_n);$ 
12:     $\tilde{B}^k \leftarrow \alpha B_{max}^k + (1 - \alpha) B_{min}^k;$ 
13:  end for
14:  return  $A^c;$ 
15: end function
16:
17: function QUAD-SELECT-LB( $I^c, P_{blr}$ )
18:    $I_{gray} \leftarrow \mathbf{rgb2gray}(I);$ 
19:    $I_q \leftarrow I_{gray};$ 
20:   while  $\frac{\text{Size}(I_q)}{\text{Size}(I_{gray})} > \epsilon_s$  do
21:     Partition  $I_q$  into four quadrants,  $I_q^1, I_q^2, I_q^3,$  and  $I_q^4;$ 
22:     Pick  $I_q^n$  with largest blurriness computed using  $P_{blr};$ 
23:      $I_q \leftarrow I_q^n;$ 
24:   end while
25:   return  $I^c(\text{Position}(I_q));$ 
26: end function

```

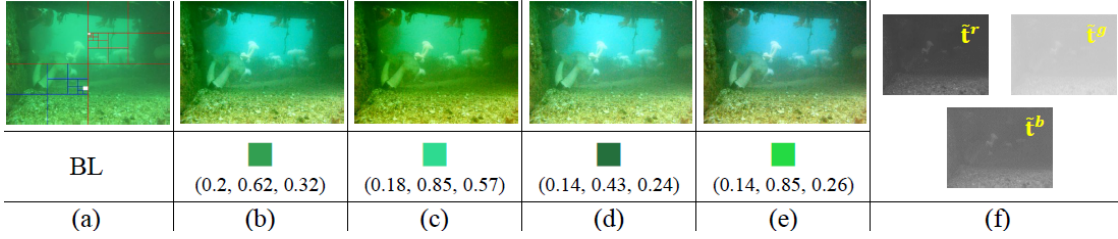


Figure 3.5: An example of ambient light estimation using Algo. 1. (a) The original image with the lowest variance and largest blurriness estimation blocks outlined in red and in blue. The white blocks are the final quadrants. The images (b)–(e) are the restored images obtained using $A_{cand_1}^c$, $A_{cand_2}^c$, $A_{cand_3}^c$, and A^c . (f) The transmissions for the red, green and blue channels estimated with A^c .

3.2.2 Depth Estimation based on Light Absorption and Image Blurriness

We propose to estimate scene depth by combining three depth estimation methods. We first define the three depth estimation methods, and then explain how they are sigmoidally combined based on the lighting and image conditions where each performs best.

The red channel map R is defined as:

$$R(\mathbf{x}) = \max_{\mathbf{y} \in \Omega(\mathbf{x})} I^r(\mathbf{y}). \quad (3.7)$$

We obtain a first estimate of depth, denoted \tilde{d}_R , directly from the red channel map by assuming that scene points which preserve more red light are closer to the camera:

$$\tilde{d}_R = 1 - F_s(R), \quad (3.8)$$

where F_s is a stretching function:

$$F_s(\mathbf{V}) = \frac{\mathbf{V} - \min(\mathbf{V})}{\max(\mathbf{V}) - \min(\mathbf{V})}, \quad (3.9)$$

where \mathbf{V} is a vector. Some successful examples are shown in Fig. 3.6(a)–(d).

Our second estimate of depth is

$$\tilde{d}_D = 1 - F_s(D_{mip}), \quad (3.10)$$

which uses the prior D_{mip} and (3.9). This depth map assumes that, for a scene point, a greater value of red light minus the maximum of green and blue lights means the point is closer to the camera. This concept was first proposed in [19], where D_{mip} was used to estimate transmission, rather than the depth directly.

Our third approach is to use the image blurriness P_r in Eq. (3.2) to estimate depth:

$$\tilde{d}_B = 1 - F_s(C_r(P_r)). \quad (3.11)$$

Combining Eq. (3.8), Eq. (3.10), and Eq. (3.11), we propose to estimate underwater scene depth based on light absorption and image blurriness according to the estimated ambient light A^c and the average input red value:

$$\tilde{d}_n(\mathbf{x}) = \theta_b [\theta_a \tilde{d}_D(\mathbf{x}) + (1 - \theta_a) \tilde{d}_R(\mathbf{x})] + (1 - \theta_b) \tilde{d}_B(\mathbf{x}), \quad (3.12)$$

where $\theta_a = S(\mathbf{avg}_c(A^c), 0.5)$ and $\theta_b = S(\mathbf{avg}(I^r), 0.1)$ are determined by the sigmoid function defined in Eq. (3.6). Finally, the depth map is refined and smoothed by either soft matting [32] or guided filtering [33]. The estimated depth map $\tilde{d}_n \in [0, 1]$ can be regarded as a map of normalized relative distance for the scene points of the input image.

The explanation for this combined approach is as follows. When the image has some reasonable level of red content overall ($\mathbf{avg}(I^r) \gg 0.1$) and the ambient light is relatively dim ($\mathbf{avg}_c(A^c) \ll 0.5$) then \tilde{d}_R alone represents depth well. In this case, $\theta_a \approx 1$ and $\theta_b \approx 1$, and $\tilde{d}_n(\mathbf{x}) \approx \tilde{d}_R(\mathbf{x})$. As the ambient light gets brighter, the possibility that

$\tilde{d}_R(\mathbf{x})$ fails to represent scene depth gets higher. Because the ambient light accounts for more of the observed intensity for a scene point farther from the camera, far scene points may still have large values in the red channel and be wrongly judged as being close according to Eq. (3.8), as seen in Fig. 3.6 (e)–(f).

When an underwater image has a brighter ambient light, we find that \tilde{d}_D is more reliable to represent scene depth. The red light of a farther scene point is absorbed more compared to the green and blue light, shown in Fig. 3.6 (c)–(f). So when the image has some reasonable level of red content overall ($\mathbf{avg}(I^r) \gg 0.1$) and the ambient light is relatively bright ($\mathbf{avg}_c(A^c) \gg 0.5$) then \tilde{d}_D alone represents depth well. In this case, $\theta_a \approx 0$ and $\theta_b \approx 1$, and $\tilde{d}_n(\mathbf{x}) \approx \tilde{d}_D(\mathbf{x})$.

Lastly if there is very little red light in the scene, so $\mathbf{avg}(I^r) \ll 0.1$, then both Eq. (3.8) and Eq. (3.10) which directly use red channel values are likely to fail to estimate scene depth properly. In this case, $\theta_b \approx 0$, and $\tilde{d}_n(\mathbf{x}) \approx \tilde{d}_B(\mathbf{x})$ mean that the depth estimation reverts to using the blurriness map alone, as in Section 3.1. In between these various extremes, the depth map comes from a weighted combination of the three approaches.

3.2.3 Transmission Estimation and Scene Radiance Recovery

As described in Section 2.1, the transmission estimation of the DCP-based methods is based on Eq. (2.3). By contrast, we calculate the transmission maps according to Eq. (2.1), which uses the depth from the camera to scene points. To measure the distance from the camera to each scene point, the distance d_0 between the closest scene point and the camera must be estimated as well. Via the maximum difference between the estimated A^c and the observed intensities I^c in the input image, the estimated $\tilde{d}_0 \in [0, 1]$ can be calculated by:

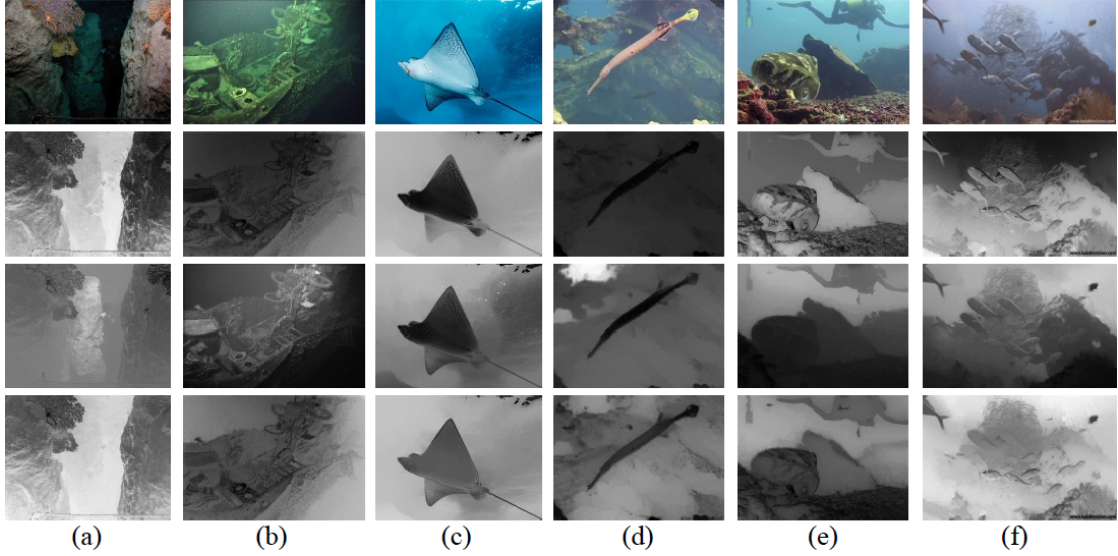


Figure 3.6: Examples of depth estimation based on light absorption and image blurriness. The original images are in the first row. The depth maps obtained based on the red channel R , D_{mip} , and P_{blr} are in the second, third, and fourth rows. The means of the estimated ambient light $\text{avg}_{c \in \{r,g,b\}}(A^c)$ in the column (a)–(f) are 0.06, 0.18, 0.5, 0.53, 0.62, and 0.81. The original image (b) is from [68], and (d)–(f) are from [59].

$$\tilde{d}_0 = 1 - \max_{x, c \in \{r,g,b\}} \frac{|A^c - I^c(\mathbf{x})|}{\max(A^k, 1 - A^k)}, \quad (3.13)$$

where $k = \mathbf{argmax}_{c \in \{r,g,b\}} (\max_x |A^c - I^c(\mathbf{x})|)$. If ambient light accounts for a large portion of the observed intensities for the closest scene point, the maximum difference would be small, and \tilde{d}_0 would be large, *i.e.*, the distance from the camera to the closest object in the scene is long. Combining Eq. (3.12) and (3.13), the final scene depth map \tilde{d}_f is given by:

$$\tilde{d}_f(\mathbf{x}) = D_\infty \times (\tilde{d}_n(\mathbf{x}) + \tilde{d}_0), \quad (3.14)$$

where D_∞ is a scaling constant for transforming the relative distance to the actual distance.

With \tilde{d}_f , we can calculate the transmission map for the red channel as:

$$\tilde{t}^r(\mathbf{x}) = e^{-\beta^r \tilde{d}_f(\mathbf{x})}, \quad (3.15)$$

where $\beta^r \in [\frac{1}{8}, \frac{1}{5}]$ for Ocean Type-I water [3, 14, 52]. Roughly 98% of the world's open ocean and coastal waters fall into this category [50]. Then, we can compute the transmission maps, \tilde{t}^g and \tilde{t}^b , for the green and blue channels by Eq. (2.7) and Eq. (2.8). Note that the typical ranges of the wavelength of red, green and blue light are $\lambda^r = 620 \sim 750 \text{ nm}$, $\lambda^g = 490 \sim 550 \text{ nm}$, and $\lambda^b = 400 \sim 490 \text{ nm}$. We choose three standard wavelengths for red, green and blue light $\lambda^r = 620 \text{ nm}$, $\lambda^g = 540 \text{ nm}$, and $\lambda^b = 450 \text{ nm}$, as used in [17]. We found that the restoration results are not sensitive to values of $\beta^r \in [\frac{1}{8}, \frac{1}{6}]$, and we set $\beta^r = \frac{1}{7}$. We also set $D_\infty = 8 \text{ m}$ for Eq. (3.14), so the range of \tilde{t}^r is $[0.1, 1]$. Fig. 3.5(f) gives an example of transmission maps for the red, green and blue channels of a greenish underwater image based on Eq. (2.8) and Eq. (3.15). We can see that with properly estimated ambient light and our parameters, the UIBLAR method can well restore the image as shown in Fig. 3.5(e).

At the end, we recover the scene radiance using Eq. (2.6). Fig. 3.7 gives an example to show the effectiveness of using transmission estimation considering \tilde{d}_0 for Eq. (3.14) in our method. Our method with \tilde{d}_0 produces a more satisfactory restored result with better contrast and saturated color.

The proposed depth estimation based on light absorption can also handle artificial lighting gracefully. If ambient light of an underwater image with artificial lighting is dim, the restoration using the depth map derived by the red channel map R in Eq. (3.7) would regard those bright pixels as being close and not over-compensate their color. When ambient light is bright, the red light from the background pixels would attenuate more than that of the foreground pixels, which could be correctly interpreted as scene depth using Eq. (3.10). Sec. 3.2.4 will demonstrate restoration examples with artificial lighting.

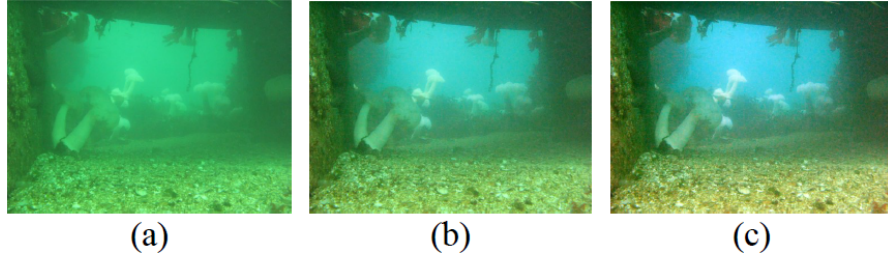


Figure 3.7: An example of transmission estimation with and without \tilde{d}_0 . (a) Original image, and its restored images obtained using the proposed UIBLAR method, where transmission estimation (b) does not consider \tilde{d}_0 and (c) considers $\tilde{d}_0 = 0.68$.

3.2.4 Experimental Results

Previous underwater image restoration methods used the IFM in Eq. (1.1) only based on the DCPs or the MIP. In this section, we compare our UIBR method in Section 3.1 and the UIBLAR against the DCP- and the MIP-based methods. The performance of all the compared methods is evaluated in three ways:

1. Subjective visual comparison including examination of the depth map and the ambient light,
2. Objective quantitative full-reference assessment of restored synthesized underwater images, and
3. Objective quantitative no-reference quality assessment of restored real-world underwater images.

3.2.4.1 Qualitative Assessment

In the visual comparison, we use six underwater images with different underwater color tones and lighting conditions for testing, where the depth maps shown all undergo a simple individual contrast stretching step for display.

In Fig. 3.8, we can see that the original image looks hazy and has bright ambient light. All methods work well for this case. The UIBR approach and the UIBLAR method

generate similar depth maps and ambient light to those obtained by the DCP and MIP methods [16, 17, 19, 34]. All of the result images look restored and enhanced although some color differences exist.

In contrast, the original image in Fig. 3.9 is dimly lit, which invalidates the DCPs and MIP. Results from the MIP-based [19] and DCP-based methods [16, 17, 34] look insignificantly restored because of the incorrect depth map and wrong ambient light selection from the bright foreground pixels. The UIBR method (Section 3.1) and the UIBLAR method (Section 3.2) estimate the scene depth and ambient light more correctly.

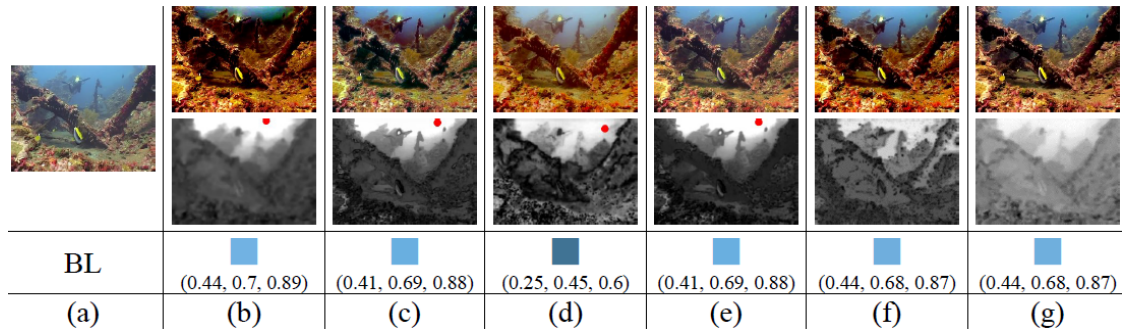


Figure 3.8: A restoration example where all methods are successful. (a) The original image. The enhanced results, and the corresponding depth map and ambient light (marked with a red dot for (b)–(e)) obtained using: (b) [19], (c) [34], (d) [16], (e) [17], (f) the UIBR method (Section 3.1), and (g) the UIBLAR method (Section 3.2).

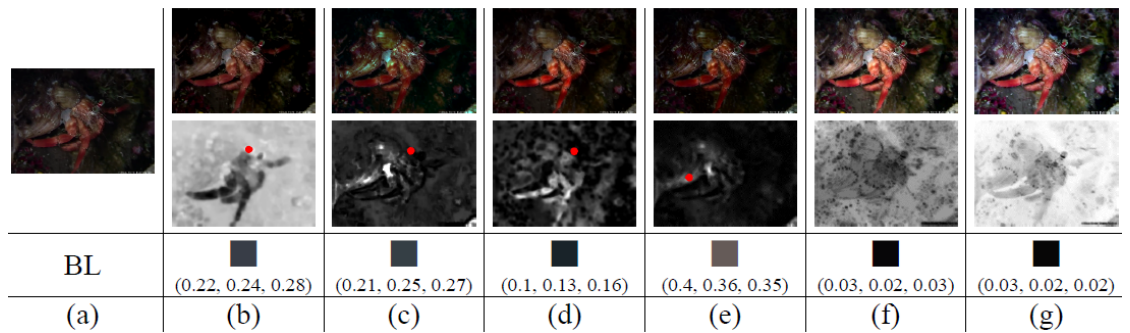


Figure 3.9: An example of restoring an underwater image with dim ambient light. (a) The original image. The restored results, and the corresponding depth map and ambient light (marked with a red dot for (b)–(e)) obtained using: (b) [19], (c) [34], (d) [16], (e) [17], (f) the UIBR method (Section 3.1), and (g) the UIBLAR method (Section 3.2).

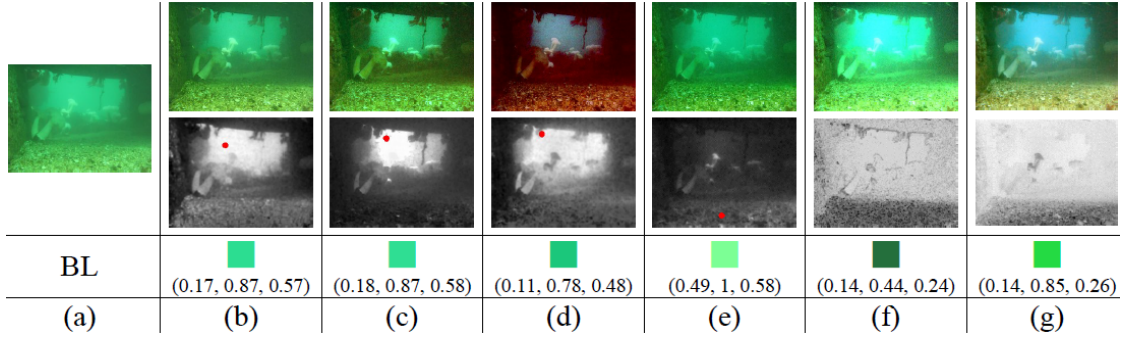


Figure 3.10: An example of restoring a greenish underwater image. (a) The original image. The restored results, and the corresponding depth map and ambient light (marked with a red dot for (b)–(e)) obtained using: (b) [19], (c) [34], (d) [16], (e) [17], (f) the UIBR method (Section 3.1), and (g) the UIBLAR method (Section 3.2).

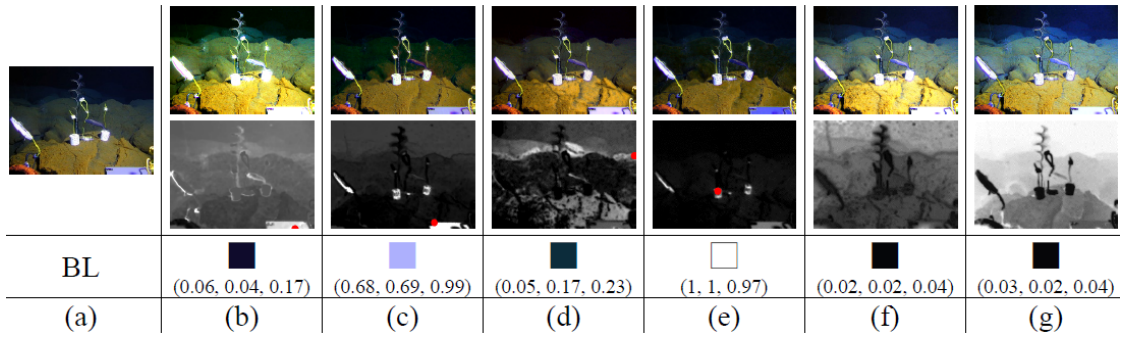


Figure 3.11: An example of restoring an underwater image with artificial lighting. (a) The original image. The restored results, and the corresponding depth map and ambient light (marked with a red dot for (b)–(e)) obtained using: (b) [19], (c) [34], (d) [16], (e) [17], (f) the UIBR method (Section 3.1), and (g) the UIBLAR method (Section 3.2). The original image comes from [68].

Fig. 3.10 gives an example of restoring a greenish underwater image, which has some bright pixels in the foreground and dark pixels in the background, making the DCPs invalid. The depth map based on I_{dcp}^{rgb} [17] is opposite to the scene depth, resulting in a wrong ambient light selection and a poor restoration. For the method based on I_{dcp}^{gb} [34], even though the ambient light is properly selected, it presents an unsatisfactory restoration result because most of the pixels are mistakenly regarded as being close. The methods based on MIP [19] and $I_{dcp}^{r'gb}$ [16] both erroneously consider some foreground pixels as being far and background pixels as being close, also failing to restore the

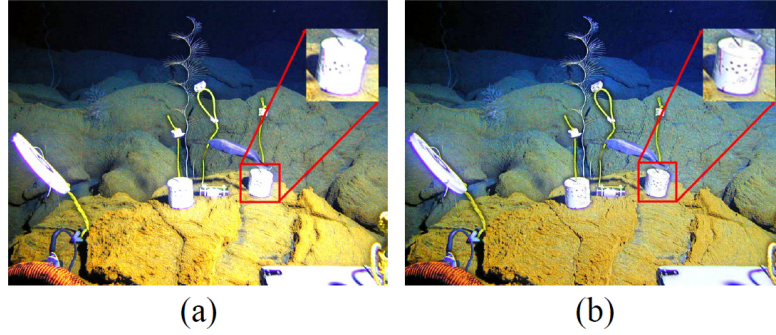


Figure 3.12: A close comparison between (a) the UIBR method (Section 3.1) and (b) the UIBLAR method (Section 3.2) for the original image shown in Fig. 3.11.

image. The UIBR method (Section 3.1), which estimates depth more accurately in this case, gives an overexposed restoration result because of selecting dimmer ambient light. Additionally, like [19] and [34], it estimates only one single transmission map without considering different attenuation levels for RGB channels. Thus, their output images cannot be properly restored. The proposed UIBLAR method correctly estimates the depth and ambient light, and thus generates more accurate transmission maps for the red, green, and blue channels. Using these transmission maps (shown in Fig. 3.5(f)), our UIBLAR method (Section 3.2) compensates more red and blue light for the original image than green light.

Fig. 3.11 shows an example of restoring an underwater image shot with artificial lighting. The method based on I_{dcp}^{rgb} [17] wrongly regards almost all of the pixels in the image as being close except for the white objects, leading to a restored image nearly identical to the original. The I_{dcp}^{gb} method [34] picks a bright foreground pixel as ambient light, which makes the background even darker. The $I_{dcp}'^{gb}$ [16] method also produces a restored image with a dimmer background because of the incorrect depth and ambient light estimation. Although the MIP-based [19] method selects dark ambient light to reveal the background scene in the processed image, it also produces an overexposed foreground. As shown in Fig. 3.12, the UIBR method produces a good result for the

background by estimating there is a dark ambient light but also overexposes some smooth regions in the foreground for which depth estimated based on blurriness is inaccurate. Our UIBLAR method estimates ambient light and depth more precisely and generates a well-enhanced restored image. We can see from the depth map that the bright pixels in the original image are regarded as being close, which prevents their overexposure.

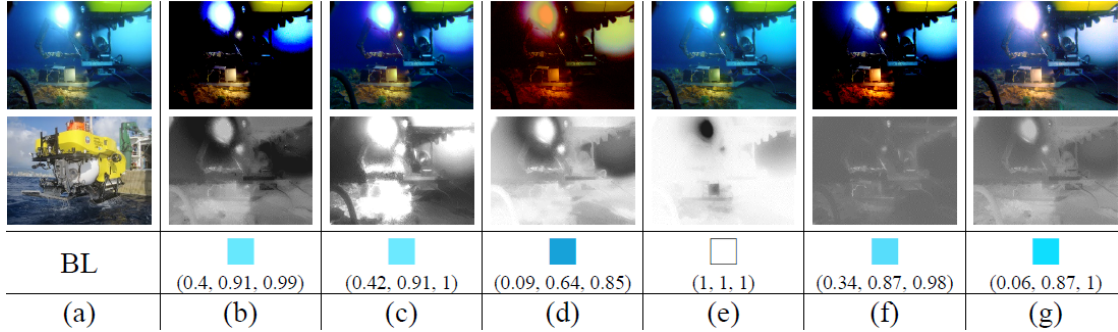


Figure 3.13: A restoration example involving artificial lighting. (a) An underwater image of *Pisces V* and its out-of-water image. The restored results, and the corresponding **transmission map** (only \tilde{t} is shown for [17] and our UIBLAR method) and ambient light obtained using: (b) [19], (c) [34], (d) [16], (e) [17], (f) the UIBR method (Section 3.1), and (g) the UIBLAR method (Section 3.2). The original image is from [68].

Lastly, Fig. 3.13 demonstrates restoration of a special case with artificial lighting. Fig. 3.13(a) shows an image of *Pisces V* [57], a deep-submergence vehicle, with its external light on in the underwater scene, as well as its out-of-water image for comparison. The red light in the underwater image is attenuated more than green and blue light. Unlike Fig. 3.8–Fig. 3.11 that present the depth maps, we show the corresponding transmission map estimated by each of the compared methods for the processed image to better explain the restoration results. Note that scene transmission aims to describe the portion of the scene radiance not scattered or absorbed but reaching the camera. A larger value in a transmission map means the corresponding scene point has more scene radiance that reaches the camera, while a smaller value means the ambient light accounts for more of the observed intensity of that scene point. Hence, the transmission map for the underwater

image in Fig. 3.13(a) should have larger values for scene points closer to the artificial light and smaller values for the points farther from the light.

In Fig 3.13(c)–(f), the methods based on the I_{dcp}^{gb} [34], I_{dcp}^{rgb} [16], I_{dcp}^{rgb} [17], and image blurriness [36] described in Section 3.1 fail to generate such transmission maps, and produce poor restoration results. The MIP-based method [19] estimates transmission well, yet its estimated ambient light that has a larger value in the red channel is inaccurate, leading to a dimmer restoration result. The proposed UIBLAR method attains a more accurate transmission map and ambient light selection and presents a more precise color restoration result.

3.2.4.2 Quantitative Assessment

In the quantitative assessment, we evaluate all the compared methods using synthetic underwater images and real-world underwater images.

First, although the simplified IFM in Eq. (1.1) is widely used to describe the formation of a hazy image and can also be invoked to explain the formation of an underwater image, light that travels through water causes image blur because of light scattering and refraction [43], which is ignored by this model. To synthesize a more realistic underwater image, image blur must be incorporated in the model. This image blur can be modeled by a point spread function, where the blur kernel width is proportional to the scene depth [43, 48, 49]. Combining the IFM and the point spread function, we describe an underwater IFM as:

$$I^c(x) = [J^c(x)t^c(x) + A^c(1 - t^c(x))] * \Phi(\beta^c, d(x)), \quad (3.16)$$

where Φ is a point spread function of the form [48]:

$$\Phi(\beta, z) = (e^{-\gamma z} - e^{-\kappa z})e^{-a\frac{\|\mathbf{x}_z\|^2}{z}}, \quad (3.17)$$

where $a > 0$ and $|\gamma| \leq \kappa$ are empirical constants, and \mathbf{x}_z is the coordinate for the point spread function.

In the quantitative analysis, we first synthesize underwater images for evaluation. Five ground truth images, for which the depth maps are known, were used to synthesize underwater images using Eq. (3.16). We focus initially on an indoor image “reindeer,” which was used in [53] to synthesize a hazy image. The image and its depth map are shown in Fig 3.14(a). In this image, the foreground pixels are not bright, so it will not tend to invalidate the DCP and MIP assumptions. Thus, it is useful for testing the capability of the compared methods to restore underwater images with different ambient light. For a fair comparison, all of the compared methods use the 7×7 local patch $\Omega(x)$, a lower bound $t_0 = 0.1$ for the TM in Eq. (2.6), and the guided filtering to smooth the transmission map. To compare the color restoration results, we adopt two metrics, PSNR and SSIM.

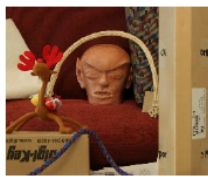
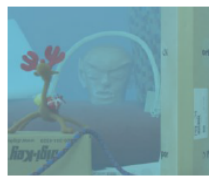
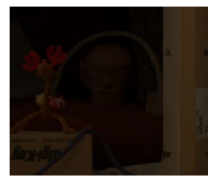
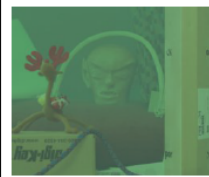
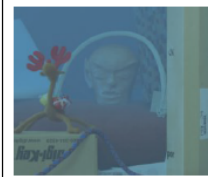
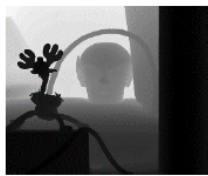




Original	Tone I	Tone II	Tone III	Tone IV
				
	 (0.41, 0.73, 0.88)	 (0, 0, 0)	 (0.3, 0.59, 0.39)	 (0.29, 0.5, 0.71)
(a)	(b)	(c)	(d)	(e)

Figure 3.14: Examples of synthesizing underwater images with four different underwater color tones using Eq. (3.16). (a) The ground truth image and its depth map. (b)–(e) Synthesized underwater images with $d_0 = 4$ and $r_s = 4$.

The ground truth image, denoted J_g , its ground truth depth map, $d_g \in [0.6, 3.1 \text{ m}]$, and four ambient lights are used to simulate underwater images with four different underwater color tones, shown in Fig. 3.14. For each color tone, we modify the depth

map in two test modes to adjust the relative amounts of ambient light and scene radiance in the synthesized observed intensity. The first test mode, “TestMode–InitD,” adds an initial distance d_0 to the ground truth depth: $d_0 + d_g = d_s$, where d_s is the final depth map used in the synthesis, and d_0 takes values in the set $\{4, 5, 6, 7, 8\}$ for testing. The second test mode, “TestMode–ScaleD,” increases the scene depth by multiplying by a scaling factor: $d_s = d_f + d_g \times r_s$, where $d_f = 4$ is a fixed initial distance, and $r_s \in \{1, 2, 3, 4, 5\}$.

The transmission map for the red channel is calculated by $t^r(x) = e^{-\beta_s^r d_s(x)}$ as Eq. (2.1) with $\beta_s^r = \frac{1}{5}$, and the transmission maps for the green and blue channels are estimated by Eq. (2.7) and Eq. (2.8) based on the chosen ambient light. For the point spread function in Eq. (3.17), we set $\gamma = \frac{\beta}{2}$, and $a = 8$. By putting J_g , t^c and A^c into Eq. (3.16), we can synthesize underwater images. Examples are shown in Fig. 3.15.

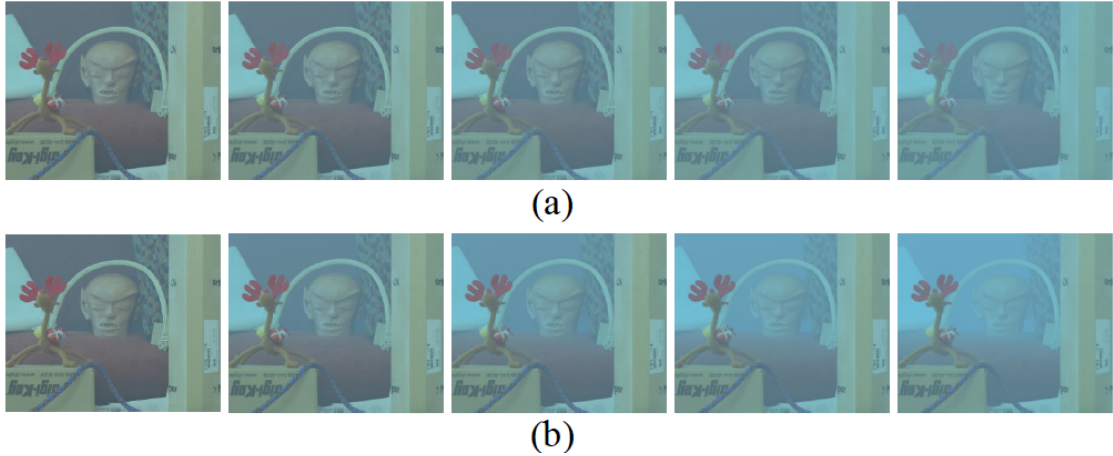


Figure 3.15: All test synthesized underwater images with Tone I color. The images from left to right are synthesized (a) using $d_0 = 4, 5, \dots, 8$ in “TestMode–InitD” and (b) using $r_s = 1, 2, \dots, 5$ in “TestMode–ScaleD.”

For each test mode, we compute the PSNR and SSIM results between the ground truth image J_g and the synthesized underwater images restored using the five IFM-based restoration methods [16, 17, 19, 34, 36], and the proposed UIBLAR method, shown in Fig. 3.16 and Fig. 3.17. In Fig. 3.16, we see that our UIBLAR method performs better for all the four underwater color tones. As the scene depth increases, the PSNR and SSIM

results of the compared methods become close. In Fig. 3.17, the UIBLAR method is better than the other ones except for [34] in the PSNR results for Tone I and IV colors. This is because we set $D_\infty = 8 \text{ m}$ in Eq. (3.14) to restore the color of underwater objects in the range of scene depth $[0, 16 \text{ m}]$, and thus the UIBLAR method does not restore well scene points farther than this range. However, the proposed method still outperforms all the other methods in the SSIM results in “TestMode–Scaled.” Note that the UIBLAR method excels more in restoring images with Tone II color, which represents very dim ambient light. This is because dim ambient light violates the assumptions underlying the DCPs and MIP. Examples of restoring synthesized underwater images with Tone I–IV colors obtained using our UIBLAR method are in Fig. 3.18.

To measure the effectiveness of transmission estimation based on our proposed depth estimation, we compare the restoration results obtained using the TMs estimated based on the DCPs and MIP, as well as ours. That is, we adopt different TM estimation methods to generate the TM for the red channel \tilde{t}^r . The transmission maps for the green and blue channels are then estimated by Eq. (2.7) and Eq. (2.8) based on the proposed BL. We compare the restoration results obtained using these different transmission estimation methods. Table 3.1 lists average PSNR/SSIM results over all the tested d_0 and r_s obtained using our UIBLAR method and its mixed methods using other transmission estimation methods based on DCPs, MIP, or image blurriness. Namely, the column marked d_0 contains average PSNR/SSIM of the restoration results over all the test d_0 in “TestMode–InitD,” while the column marked r_s contains the results over all the test r_s in “TestMode–Scaled.” We can see that the proposed transmission estimation outperforms the others.

Moreover, we demonstrate the average PSNR and SSIM results for all the compared methods in Table 3.2 and Table 3.3 for “TestMode-InitD” and “TestMode-Scaled.” We also show the results attained using the exact ambient light and transmission map in

the compared methods in order to further analyze the preciseness of the ambient light and transmission estimation methods, individually. In Table 3.2, we see the superiority of the proposed UIBLAR method in each compared category. In Table 3.3, the UIBLAR method is better in all the tested underwater color tones on average except for Tone I color, which represents bright blue BL, where it incurs small PSNR deficits compared to [19] in the category of the exact transmission map and [34] in that of the exact ambient light.

In addition to “reindeer”, three more images with ground truth depth maps were selected from [53] to synthesize underwater images with six different ambient lights (two for each image), as shown in Fig. 3.19. The ground truth depth d_g for the three images, “lawn,” “flower,” and “road,” are in the range $[0.4, 11.3 \text{ m}]$, $[0.5, 13.2 \text{ m}]$, $[0.3, 9.5 \text{ m}]$, respectively. To vary the initial distance d_0 for each image, we set $d_0 \in \{1, 2, \dots, 5 \text{ m}\}$ for “flower,” $d_0 \in \{2, 3 \dots 6 \text{ m}\}$ for “road,” and $d_0 \in \{3, 4, \dots, 7 \text{ m}\}$ for “lawn,” while r_s still takes values in the set $\{1, 2, \dots, 5\}$. As can be seen in Tables 3.4 to 3.6, the results are generally in line with those based on “reindeer,” supporting the superiority of the UIBLAR method. Note that Table 3.6 is like Table 3.1, where the column marked d_0 contains average PSNR/SSIM results over all the test d_0 in “TestMode–InitD,” while the column marked r_s contains the results over all the test r_s in “TestMode–Scaled,” where d_f is the smallest value in their corresponding d_0 set for each test image.

Next, to evaluate performance of all the compared methods on restoring real-world underwater images, we adopt two non-reference image quality metrics. One is the Blind/Referenceless Image Spatial QUality Evaluator (BRISQUE) [24], a natural scene statistics-based distortion-generic blind/no-reference image quality assessment tool for evaluating possible losses of naturalness of an image because of the presence of distortions. The score ranges from 0 to 100, where 0 represents the best quality and 100 the worst. We download its software release from [54] for testing. The other is

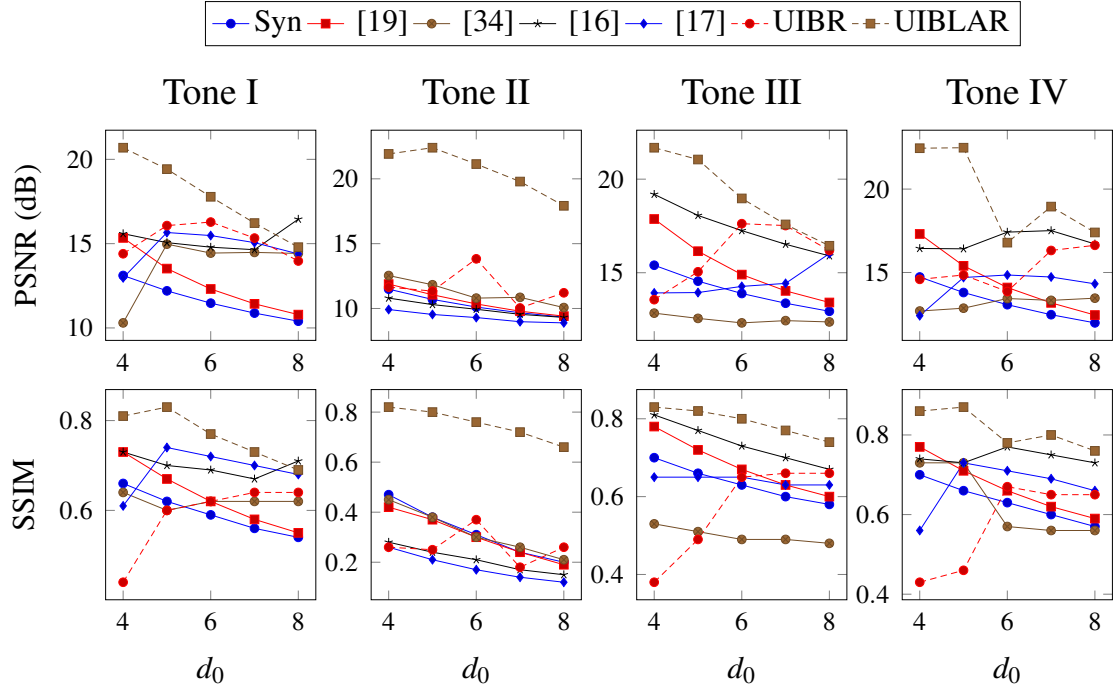


Figure 3.16: PSNR results (top) and SSIM results (bottom) obtained using different restoration methods for “TestMode-InitD.”

the Underwater Image Quality Measure (UIQM) [27]. A greater value of the UIQM represents higher image quality. In the experiment, our implementation of UIQM uses $\alpha_L = \alpha_R = 0.1$ in UICM, a 8×8 window size for the EME measure and a constant 40 for Sobel edge detection in UISM, $\mu(M) = \gamma(M) = k(M) = 1026$ for the PLIP operations in UIConM, and the default coefficients $c_1 = 0.0282$, $c_2 = 0.2952$, and $c_3 = 3.5753$.

To give an idea of output values for both metrics, Fig. 3.20 lists BRISQUE scores and UIQM values for real underwater images as well as for synthesized underwater images with different attenuation levels (for which BRISQUE scores increase and UIQM values decrease monotonically with attenuation level). In Fig. 3.21, we show 70 real underwater test images with different contents and a variety of color tones. Table 3.7 lists the average BRISQUE scores and UIQM values for the original underwater images in Fig. 3.21 and their restored images from all the compared methods. We can see that the UIBLAR method outperforms the other methods.

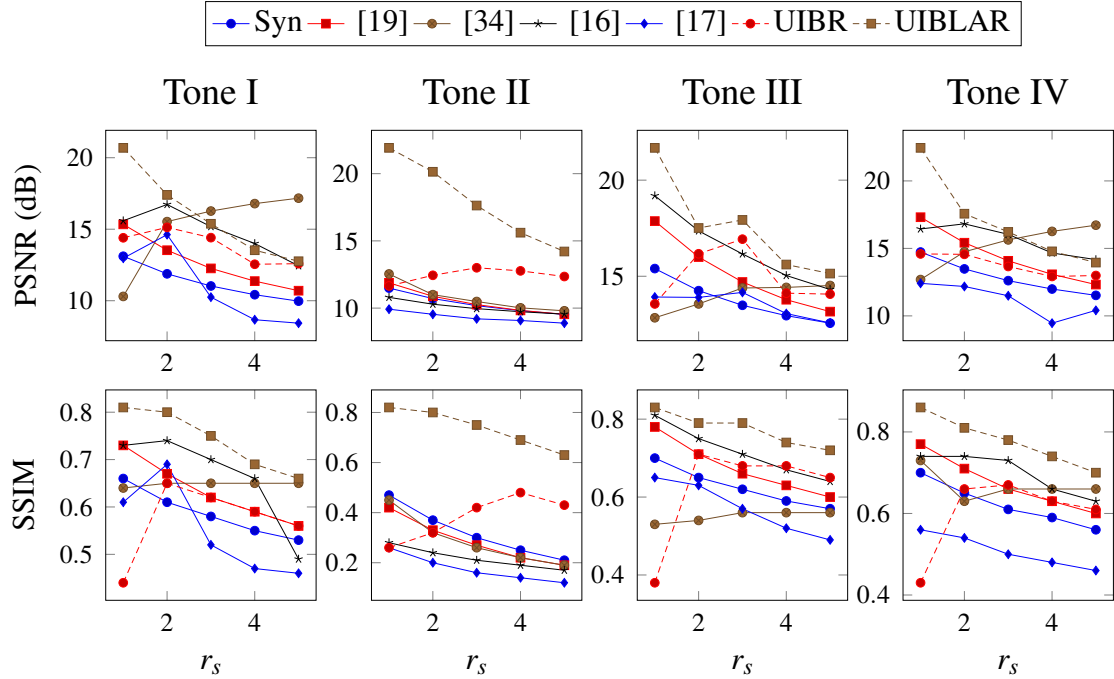


Figure 3.17: PSNR results (top) and SSIM results (bottom) obtained using different methods for “TestMode–Scaled.”

3.2.4.3 Combining IFM-based Restoration and Histogram Equalization

Methods based on the IFM, such as ours, have the goal of restoration, rather than enhancement. The previous sections aimed to demonstrate that our IFM-based method outperforms other IFM-based methods both for synthesized images (for which a ground truth is available, and full-reference fidelity metrics such as PSNR can be used), and for real underwater images (for which no-reference image quality metrics can be used).

It is also of interest to compare our IFM-based method against an underwater image enhancement method. The fusion-based enhancement method for underwater images proposed by Ancuti et al. [1] first generates two images based on the input image: one has colors adjusted by white balancing and the other is contrast-enhanced via local adaptive histogram equalization. Then these two images are fused based on their contrast, saliency, and exposure to produce the final enhanced result with better contrast and white

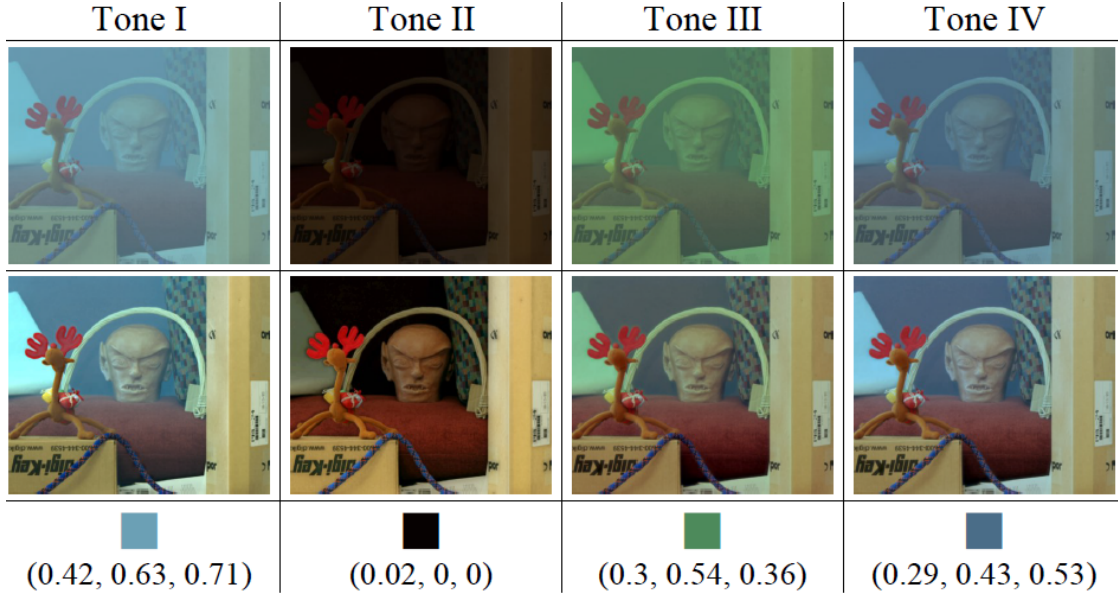


Figure 3.18: Examples of restoring synthesized underwater images with Tone I–IV colors in “TestMode–Scaled” ($r_s = 3$) obtained using the UIBLAR method. The synthesized images are in the first row, and the corresponding restored images and ambient light estimates are shown in the second and third rows.

balance.

Histogram equalization [55] is a simple contrast enhancement method that can be added as a post-processing to an IFM-based method if some application needs the contrast of an underwater image to be enhanced. In Fig. 3.22, we compare our UIBLAR method (both with and without histogram equalization contrast enhancement [56]) with the method by Ancuti et al. [1], using both subjective and objective comparisons. For objective assessment, we choose two no-reference quality assessment tools, the UIQM [27] and Underwater Color Image Quality Evaluation Metric (UCIQE) [28]. UCIQE quantifies image quality via a linear combination of the variation of chrominance, average saturation, and luminance contrast.

Fig. 3.22(a) shows the 10 original images from Emberton’s data set [35]. In Fig. 3.22(b)–(d), we see that the enhanced images via Ancuti’s method [1] (column (b)) have better contrast compared to those by our UIBLAR method (column (c)). Since

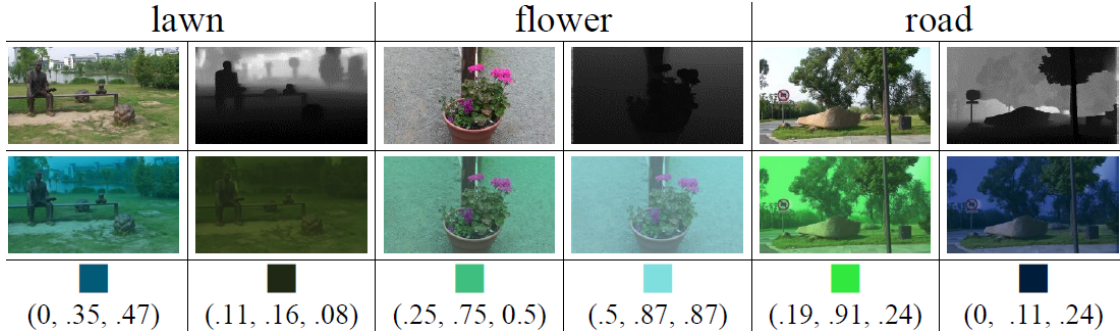


Figure 3.19: Examples of synthesized underwater images generated using three different images with their depth maps and selected ambient lights.

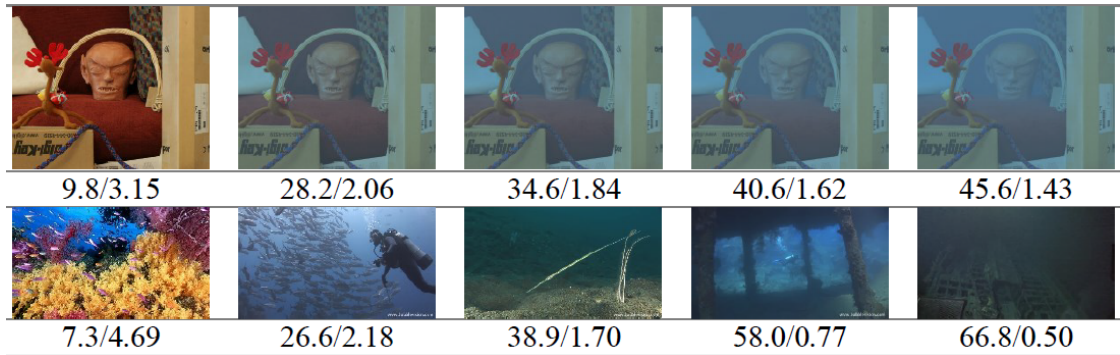


Figure 3.20: Examples of “BRISQUE score/UIQM value” pairs for synthesized (top) and real (bottom) underwater images. (The images are from [53, 59, 68], and Google Images.)

UCIQE and UIQM reward high contrast, the images obtained using [1] also have higher scores than those using our UIBLAR method. Using histogram equalization [56] on our method, the contrast and UCIQE/UIQM values go up.

Fig. 3.22(e) shows an additional 10 original images. In the top four rows of Fig. 3.22 (e)-(h), the images are very dark or have artificial lighting. The method [1] does poorly because contrast enhancement is often not effective for such images, and the white balancing of [1] sometimes introduces unwanted colors to the output images, such as the original images in the first row of Fig. 3.22 (a) and (e), which makes the processed images unnatural even though it boosts its UCIQE/UIQM scores. For the bottom six rows of Fig. 3.22 (e)-(h), since the color of the original images is more balanced, the white

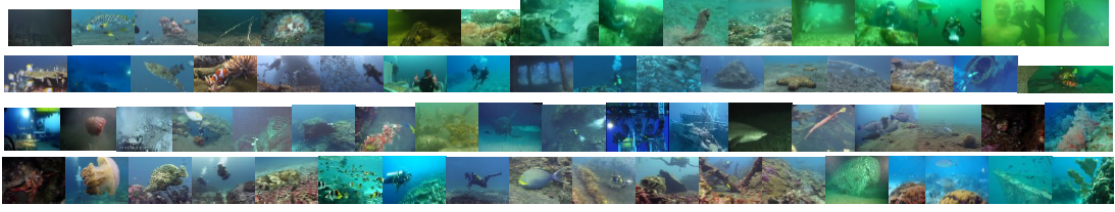


Figure 3.21: Test images for BRISQUE. (The images are from [1, 12, 16, 19, 34, 59, 68], and Google Images.)

Table 3.1: Comparison of average PSNR/SSIM of the restoration results over all the tested $d_0 \in [4, 8 m]$ and $r_s \in [1, 5]$ obtained using the UIBLAR method and its mixed methods using the TM estimation for the red channel \tilde{r}^r based on DCPs, MIP, or image blurriness.

Method	Tone I		Tone II		Tone III		Tone IV	
	d_0	r_s	d_0	r_s	d_0	r_s	d_0	r_s
UIBLAR+MIP	12.3/.62	12.0/.62	10.7/.36	10.9/.37	14.8/.67	14.5/.66	13.9/.66	13.5/.66
UIBLAR+DCP _{rgb}	15.5/.76	15.2/.75	13.0/.63	10.4/.56	13.8/.70	13.2/.71	14.8/.75	13.5/.73
UIBLAR+DCP _{gb}	16.8/.76	15.1/.70	13.1/.65	10.4/.58	16.4/.73	13.7/.70	17.1/.73	13.4/.69
UIBLAR+DCP _{r^rgb}	16.2/.77	15.5/.76	13.8/.65	12.6/.61	15.2/.73	14.9/.75	17.2/.79	15.1/.77
UIBLAR+P _{blr}	14.2/.56	13.1/.57	13.0/.58	11.8/.60	13.8/.64	13.5/.66	15.3/.65	13.4/.65
UIBLAR	17.8/.77	16.0/.74	20.6/.75	17.9/.74	19.1/.79	17.6/.78	19.6/.81	17.0/.78

balancing has little effect on these images. In comparison, the restored and enhanced results via our UIBLAR method with and without histogram equalization look better for such images.

Comparing image enhancement methods using UCIQE and UIQM or other no-reference metrics is difficult because the metrics weight contrast and colorfulness differently. For example the UIQM algorithm removes the 10% of pixels with brightest and darkest values before computing the image colorfulness, whereas the UCIQE algorithm uses all pixels. Depending on factors like this and the weight given to different components, a white balancing step or a histogram equalization step can have a significant effect on the quantitative output of the metrics.

Table 3.2: Comparison of average PSNR/SSIM of the restoration results over all the tested $d_0 \in [4, 8 m]$ for “TestMode–InitD.”

Method	Tone I			Tone II			Tone III			Tone IV		
	d_0	ExtAL [†]	ExtTM [†]	d_0	ExtAL	ExtTM	d_0	ExtAL	ExtTM	d_0	ExtAL	ExtTM
None	11.6/.59	–/–	–/–	10.3/.32	–/–	–/–	14.0/.63	–/–	–/–	13.2/.63	–/–	–/–
[19]	12.7/.63	13.0/.63	19.2/.60	10.5/.31	10.8/.37	16.6/.55	15.3/.68	15.3/.68	14.5/.43	14.5/.67	14.7/.67	15.7/.48
[34]	13.7/.62	19.9/.73	18.1/.64	11.2/.32	12.4/.65	14.5/.44	12.5/.50	19.3/.69	14.5/.43	13.2/.63	17.8/.72	16.4/.61
[16]	15.3/.70	10.6/.27	12.2/.71	10.0/.21	13.4/.56	10.6/.24	17.4/.74	13.9/.57	19.9/.70	16.9/.74	12.5/.47	18.6/.59
[17]	14.7/.69	18.1/.75	16.8/.53	9.3/.18	11.1/.29	8.7/.08	14.5/.64	16.9/.75	14.5/.40	14.2/.67	18.7/.77	13.8/.39
UIBR	15.2/.59	15.2/.48	18.1/.79	11.6/.26	14.1/.66	12.4/.33	16.0/.57	17.8/.64	19.1/.64	15.2/.57	16.5/.54	18.1/.69
UIBLAR	17.8/.77	20.8/.80	19.3/.81	20.6/.75	22.7/.89	23.3/.77	19.1/.79	23.6/.85	24.7/.83	19.6/.81	22.2/.84	26.3/.87

[†] ExtAL and ExtTM represent restoration with the exact ambient light and transmission map.

Table 3.3: Comparison of average PSNR/SSIM of the restoration results over all the tested $r_s \in [1, 5]$ for “TestMode–Scaled.”

Method	Tone I			Tone II			Tone III			Tone IV		
	r_s	ExtAL [†]	ExtTM [†]	r_s	ExtAL	ExtTM	r_s	ExtAL	ExtTM	r_s	ExtAL	ExtTM
None	11.3/.59	–/–	–/–	10.3/.32	–/–	–/–	13.7/.63	–/–	–/–	12.9/.62	–/–	–/–
[19]	12.6/.63	12.9/.64	21.4/.71	10.5/.29	10.9/.38	13.1/.39	15.1/.68	15.1/.67	17.1/.56	14.4/.67	14.5/.67	18.4/.59
[34]	15.2/.65	19.3/.71	19.9/.74	10.8/.29	10.3/.57	12.6/.37	13.9/.55	17.0/.65	16.6/.54	15.2/.67	17.6/.70	19.0/.67
[16]	14.8/.66	10.6/.28	11.0/.70	10.1/.22	13.2/.53	10.5/.24	16.4/.72	13.8/.59	20.2/.68	15.6/.70	12.5/.47	20.5/.68
[17]	11.0/.55	17.1/.73	12.7/.49	9.3/.18	11.3/.30	8.8/.09	13.5/.57	16.1/.72	13.1/.35	11.2/.51	17.7/.75	11.7/.42
UIBR	13.8/.57	14.4/.46	18.7/.78	12.4/.38	13.2/.63	18.4/.57	15.0/.62	16.8/.63	20.4/.78	13.7/.60	15.8/.54	19.0/.77
UIBLAR	16.0/.74	18.7/.77	18.3/.78	17.9/.74	18.5/.81	24.8/.79	17.6/.78	20.9/.81	22.2/.82	17.0/.78	20.2/.80	21.7/.82

[†] ExtAL and ExtTM represent restoration with the exact ambient light and transmission map.

3.3 Acknowledgement

This chapter, in full, is a reprint of two published papers, Y.-T. Peng and P. C. Cosman, “Underwater Image Restoration based on Image Blurriness and Light Absorption,” *IEEE Trans. Image Process.*, vol. 26, no. 4, pp. 1579-1594, Apr. 2017, and Y.-T. Peng, X. Zhao and P.C. Cosman, “Single Underwater Image Enhancement using Depth Estimation based on Blurriness,” *IEEE Int. Conf. on Imag. Process. (ICIP)*, pp. 4952-4956, Sep. 2015. The dissertation author was the primary investigator and author of these papers.

Table 3.4: Comparison of average PSNR/SSIM of the restoration results over all the tested d_0 for “TestMode–InitD.”

Method	lawn ■			lawn ■			flower ■			flower ■			road ■			road ■		
	d_0	ExtAL	ExtTM	d_0	ExtAL	ExtTM	d_0	ExtAL	ExtTM	d_0	ExtAL	ExtTM	d_0	ExtAL	ExtTM	d_0	ExtAL	ExtTM
None	19.4/66	–/–	–/–	13.2/48	–/–	–/–	19.1/71	–/–	–/–	16.9/66	–/–	–/–	16.7/66	–/–	–/–	15.3/55	–/–	–/–
[19]	18.8/68	22.0/71	18.5/74	13.1/47	13.4/49	10.1/25	21.0/79	23.2/81	18.9/79	19.1/73	19.8/73	29.6/93	19.0/70	19.9/73	16.1/57	15.0/55	16.8/60	13.8/48
[34]	12.6/49	15.6/72	17.7/70	10.7/30	11.4/65	10.1/24	15.6/72	15.9/75	23.4/89	14.1/71	14.1/69	26.0/92	13.9/55	17.7/72	14.0/45	11.7/36	12.0/68	10.9/24
[16]	11.6/37	15.9/59	23.0/85	11.6/40	16.0/64	12.3/42	10.0/49	10.7/49	24.1/90	17.3/70	7.0/19	10.3/62	10.6/22	15.4/52	14.3/46	10.7/24	19.1/78	12.6/39
[17]	17.7/64	18.7/70	11.9/40	9.8/24	11.1/56	9.0/15	11.1/67	20.6/86	10.4/54	15.8/79	19.9/91	23.2/84	15.8/55	20.6/77	11.5/29	13.7/48	14.3/59	10.4/19
UIBR	10.7/30	16.1/67	17.8/72	13.5/52	17.8/71	13.7/55	12.0/58	13.1/64	14.4/72	16.6/74	13.0/60	22.3/91	12.6/37	17.4/65	14.1/45	11.5/27	18.0/78	12.6/38
UIBLAR	22.7/79	26.5/85	24.1/87	19.0/79	20.8/83	23.2/88	24.0/89	27.8/89	26.0/91	19.3/87	24.9/89	21.3/92	22.5/84	22.4/84	26.4/91	19.8/78	23.1/85	21.5/84

† ExtAL and ExtTM represent restoration with the exact ambient light and transmission map.

Table 3.5: Comparison of average PSNR/SSIM of the restoration results over all the tested r_s for “TestMode–Scaled.”

Method	lawn ■			lawn ■			flower ■			flower ■			road ■			road ■		
	r_s	ExtAL	ExtTM	r_s	ExtAL	ExtTM	r_s	ExtAL	ExtTM	r_s	ExtAL	ExtTM	r_s	ExtAL	ExtTM	r_s	ExtAL	ExtTM
None	17.5/62	–/–	–/–	13.0/45	–/–	–/–	16.9/62	–/–	–/–	16.0/58	–/–	–/–	14.8/60	–/–	–/–	14.6/49	–/–	–/–
[19]	17.9/64	20.1/66	15.9/63	12.9/45	13.1/46	10.9/32	18.7/70	21.5/71	17.8/76	18.2/64	18.6/64	28.2/85	17.3/65	18.5/66	17.4/63	14.3/49	15.8/53	12.7/40
[34]	12.3/45	14.9/66	15.6/62	10.8/31	10.7/54	10.3/27	15.3/70	14.9/71	22.5/83	14.5/68	14.2/66	25.2/85	15.4/58	16.8/64	17.0/61	11.6/34	12.2/58	11.0/25
[16]	11.8/37	15.3/55	20.4/78	10.8/33	15.0/58	11.3/35	9.3/41	10.0/42	23.3/84	11.1/41	7.0/17	9.7/53	11.7/35	14.6/46	14.6/54	13.0/37	17.5/67	13.4/46
[17]	16.7/60	17.6/66	10.9/32	9.5/21	10.7/47	8.9/14	11.0/59	21.7/80	8.8/40	14.7/69	21.3/83	18.7/71	13.5/48	18.2/69	11.4/28	13.1/43	13.6/50	10.1/18
UIBR	13.4/46	16.3/65	18.9/75	14.9/56	15.9/61	17.9/69	16.0/66	14.9/65	22.1/81	18.0/69	15.5/62	24.3/85	14.2/45	16.3/57	16.5/59	12.8/38	16.0/67	13.7/49
UIBLAR	21.1/74	23.2/79	24.2/81	17.4/71	17.9/72	21.2/77	21.2/77	23.4/77	23.5/84	19.3/75	21.8/76	22.1/84	18.6/70	19.2/72	20.8/73	17.8/67	19.2/70	18.8/74

† ExtAL and ExtTM represent restoration with the exact ambient light and transmission map.

Table 3.6: Comparison of average PSNR/SSIM of the restoration results over all the tested d_0 and r_s obtained using the UIBLAR method and its mixed methods using the TM estimation for the red channel \tilde{r} based on DCPs, MIP, or image blurriness.

Method	lawn ■		lawn ■		flower ■		flower ■		road ■		road ■	
	d_0	r_s	d_0	r_s	d_0	r_s	d_0	r_s	d_0	r_s	d_0	r_s
UIBLAR+MIP	19.8/68	18.6/64	13.3/49	13.1/46	20.9/78	19.5/68	17.9/72	17.1/63	18.5/71	16.8/64	15.9/58	15.2/52
UIBLAR+DCP _{rgb}	21.3/76	18.9/70	12.0/66	10.9/55	20.0/86	20.4/81	17.4/80	19.3/80	20.4/77	17.9/67	15.9/71	14.1/58
UIBLAR+DCP _{gb}	14.7/64	14.2/62	12.0/66	10.9/55	19.1/79	18.1/77	15.5/72	15.0/70	19.8/78	17.6/68	13.9/70	12.3/55
UIBLAR+DCP _{r-gb}	21.9/77	20.9/73	15.0/77	13.5/67	22.1/91	21.1/83	17.4/80	19.3/80	20.7/77	18.1/68	19.6/78	16.9/68
UIBLAR+P _{blr}	21.7/77	20.8/72	16.7/71	15.7/62	17.8/77	18.1/74	15.6/68	16.4/67	20.0/81	17.0/64	18.3/75	15.5/64
UIBLAR	22.7/79	21.1/74	19.0/79	17.4/71	24.0/89	21.1/77	19.3/87	19.3/75	22.5/84	18.6/70	19.8/78	17.8/67

Table 3.7: Average BRISQUE scores and UIQM values of the original images in Fig. 3.21 and their restored versions from all the compared methods.

	Original	[19]	[34]	[16]	[17]	UIBR	UIBLAR
BRISQUE	36.31	34.49	31.45	33.57	31.61	31.73	30.24
UIQM	2.60	2.83	3.05	2.65	2.75	3.17	3.23

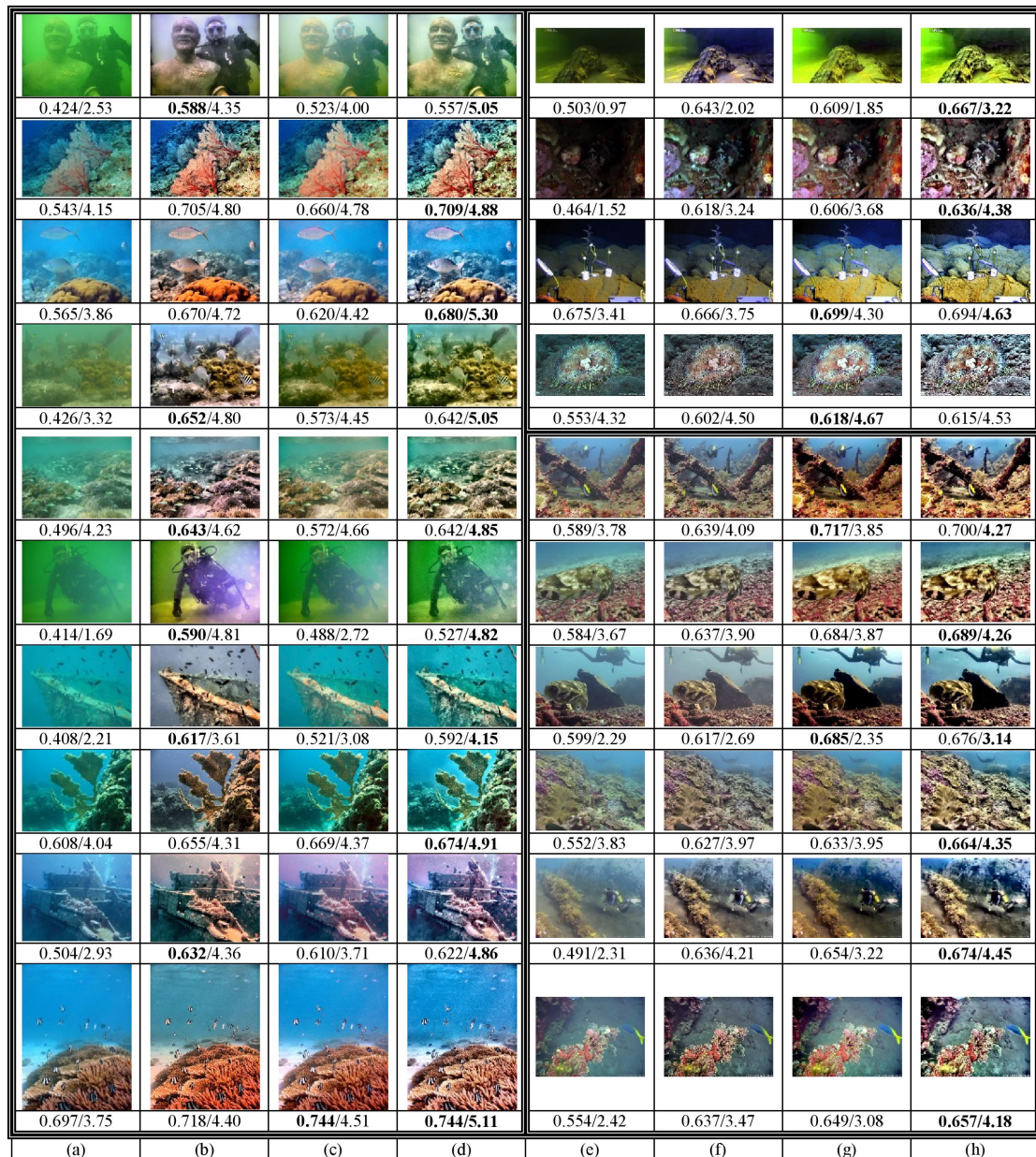


Figure 3.22: Comparisons between the processed images obtained using [1] and the UIBLAR method with and without contrast enhancement. The UCIQE score/UIQM value pair is shown below each image. (a) and (e) Original images. The processed results are obtained using (b) and (f) [1], (c) and (g) our method, and (d) and (h) the proposed method+histogram equalization (The original images in column (a) are from Emberton's data set [35] and the ones in column (e) are from [58–60].)

Chapter 4

Generalization of the Dark Channel

Prior

This chapter proposes a Generalization of the DCP (GDCP). It uses the depth-dependent color change for ambient light estimation and scene ambient light differential for scene transmission estimation, and works for images with different lighting conditions and color casts. Fig. 4.1 depicts the flowchart of the GDCP method. In Step 1, we analyze the depth-dependent color change for the input image I^c using a modified gradient map to estimate a depth map, and ambient light is estimated from the farthest regions. In Step 2, with the estimated ambient light A^c , the transmission \tilde{t}_{pro} is obtained using the scene ambient light differential. In Steps 3 and 4, adaptive color correction is incorporated into the IFM to generate output image J_ϕ^c involving both restoring scene radiance and removing color casts.

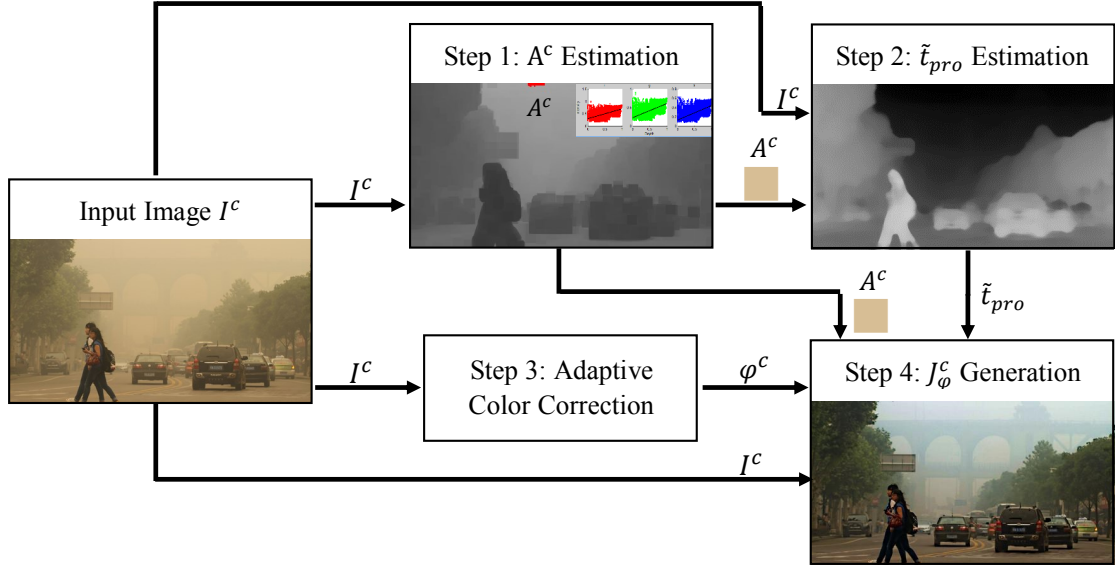


Figure 4.1: The flowchart of our GDCP method. The original image is from [11].

4.1 Ambient Light Estimation

We propose the depth-dependent color change as a means to estimate ambient light. As mentioned previously, for a hazy image, the value of the DCP for a farther scene point is generally larger than that of a closer scene point because light is more scattered by the turbid medium. Therefore, the DCP of a hazy image provides us with depth and light attenuation information, where a larger value in the DCP means that the scene point is farther and more attenuated. Based on the DCP, one of the farthest and haziest pixels in the input image is chosen to be the ambient light estimate.

The original ambient light estimation [7] using the DCP works properly for most hazy images; however, it frequently fails when we are dealing with other kinds of degraded images, such as sandstorm or underwater images with different lighting conditions and color casts that violate the underlying assumptions of the DCP. For example, for most underwater images, red light in a far scene is absorbed more than that in a closer scene so ambient light for such images often has a small value in the red

channel. In such cases, the DCP values of far scene points are frequently smaller than those of close scene points, failing to represent depth for the image and thus leading to inaccurate ambient light estimation, as can be seen in Fig. 2.2(d). If we only consider the red channel of underwater images, closer scene points may have larger values in this channel than farther scene points.

Thus, we propose to generalize the DCP based on the depth-dependent color change, which describes whether a given color channel tends to have larger or smaller values as the depth from the camera increases. For example, for an underwater image, red light usually decreases as depth increases. To describe the depth-dependent color change, a three-bit indicator $\mathbf{s} = s_r s_g s_b$ is used, where $s_c = 1$ represents that as depth increases, light for the channel c tends to increase, while $s_c = 0$ indicates that light for c tends to decrease, where $c \in \{r, g, b\}$. Thus, we have 8 different values for the indicator in total: $\mathbf{s} \in \{000, 001, \dots, 111\}$.

To determine the indicator for an image, we estimate a rough depth map D_r based on the observation that farther scene points are more blurry than closer ones, i.e., gradients of a farther scene tend to be smaller than those of a closer scene. To construct D_r , the gradient map G is first computed as $G(\mathbf{x}) = \sqrt{G_h(\mathbf{x})^2 + G_v(\mathbf{x})^2}$, where G_h and G_v are the horizontal and vertical 3×3 Sobel operators applied to the input image. Next, assuming depth in a small local patch is uniform, the modified gradient map G_m is estimated by dilating the gradient map G and filling the holes caused by smooth regions of objects using morphological reconstruction operators [42]. Then, we set $D_r(\mathbf{x}) = 1 - F_s(G_m(\mathbf{x}))$, where $F_s(G_m(\mathbf{x})) = \frac{G_m(\mathbf{x}) - \min_x(G_m)}{\max_x(G_m) - \min_x(G_m)}$ linearly stretches G_m to the range $[0, 1]$.

The relationship between depth and I^c is modeled via regression analysis: $\widehat{I}^c(\mathbf{x}) = b_c + a_c \times D_r(\mathbf{x})$, where a_c and b_c are estimated using $\mathbf{argmin}_{a_c, b_c} \sum_x (I^c(\mathbf{x}) - \widehat{I}^c(\mathbf{x}))^2$. The indicator for channel c is

$$s_c = \begin{cases} 1 & \text{if } a_c > 0; \\ 0 & \text{if } a_c \leq 0, \end{cases}$$

where $c \in \{r, g, b\}$. In addition, a larger $|a_c|$ means higher significance of the corresponding channel c to determine the scene depth. In [7], $I_{dcp}^{rgb}(\mathbf{x}) = \min_{c, \mathbf{y} \in \Omega(\mathbf{x})} I^c(\mathbf{y})$ was used as depth information for a hazy image I , where a far and a close scene point, \mathbf{x}_f and \mathbf{x}_c , generally have a relation that $I_{dcp}^{rgb}(\mathbf{x}_c) \leq I_{dcp}^{rgb}(\mathbf{x}_f)$. However, it does not hold for cases where light attenuates as the depth increases. Therefore, rather than using Eq. (2.4) as the depth map estimate for purposes of estimating ambient light, we propose to estimate a more accurate depth map D using the depth-dependent color change indicator $s_r s_g s_b$ and $|a_c|$ as:

$$D(\mathbf{x}) = \min_{c, \mathbf{y} \in \Omega(\mathbf{x})} (1 - w_c |s_c - I^c(\mathbf{y})|), \quad (4.1)$$

where $w_c = \tanh(k|a_c|)$ is the significance weighting factor for channel c , where $k = 4$ is an empirical constant. The function $\tanh(z) = \frac{e^z - e^{-z}}{e^z + e^{-z}}$ is the hyperbolic tangent, and we use it as our significance weighting function as shown in Fig. 4.3.

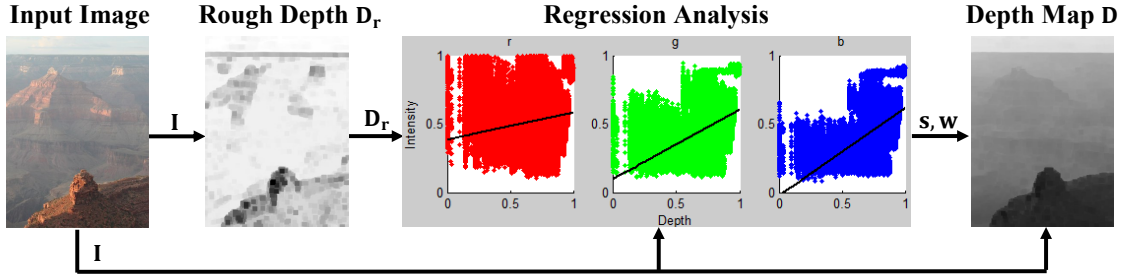


Figure 4.2: The flowchart of the depth-dependent color change determination.

Using the indicator \mathbf{s} and the significance weighting factors $\mathbf{w} = [w_r, w_g, w_b]$, we have developed a general formulation for DCP-based methods. It is found that one approach for hazy images [7], two approaches for sandstorm images [10, 11], three

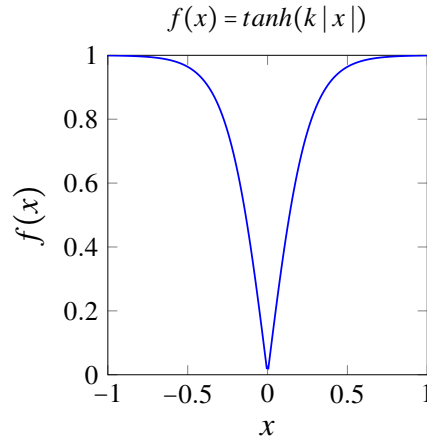


Figure 4.3: The significance weighting function.

approach for underwater images [12–16], and two approaches for night-time terrestrial images [38, 39] are all special cases of Eq. (4.1), as will be discussed later. Our formulation allows one to adjust the importance of each channel while estimating depth.

Fig. 4.4 shows comparisons of depth estimation based on the DCP [7], DCP variants [15, 16, 39], and the proposed depth estimation for degraded images with different lighting conditions and color casts. Fig. 4.4(a) shows a hazy image and its estimated depth maps. We can see that I_{dcp}^{rgb} works for the hazy image since its \mathbf{s} and \mathbf{w} indicate that the values of all three color channels, which are all significant, tend to increase as the depth increases. Fig. 4.4(b) shows an underwater image where both I_{dcp}^{rgb} and I_{dcp}^{gb} work since the image indicator $\mathbf{s} = 111$ and \mathbf{w} are similar to those for I^c in Fig. 4.4(a). However, the depth estimated using $I_{dcp}'^{gb}$ is not accurate for I^c in Fig. 4.4(b), because its $s_r = 1$ means the values of the red channel tend to increase as the depth increases but $I_{dcp}'^{gb}$, which inverts the red channel, considers the values of the red channel decrease as the depth increases. The sandstorm image in Fig. 4.4(c) has very small values in the blue channel, causing I_{dcp}^{rgb} to only consider the blue channel and to fail to produce a proper depth map. As can be seen in Fig. 4.4(d), $I_{dcp}'^{gb}$ works well for the underwater image since the values in the red channel tend to decrease and those in the green and blue channels

tend to increase as the depth increases based on its s while I_{dcp}^{rgb} , assuming an opposite tendency in the red channel, does not work at all. I_{dcp}^{gb} works somewhat imprecisely (fish is wrongly judged as being far) because it does not consider the red channel. Fig. 4.4(e) and (f) show two underwater images with artificial lighting, for which I_{dcp}^{rgb} , I_{dcp}^{gb} and $I_{dcp}^{r'gb'}$ all do poorly estimating the depth because none of them works for the case where the values in the green channel tend to decrease as the depth increases. $I_{dcp}^{r'g'b'}$ works well for cases where the values in all three color channels tend to decrease as the depth increases, such as the underwater image in Fig. 4.4(f) and the dimly-lit image in Fig. 4.4(g). The GDCP method, which incorporates the depth-dependent color change indicators and significance weighting factors, is capable of generating proper depth maps for all of these degraded images with different color change and lighting conditions.

Ambient light is estimated from the pixels of the input image that correspond to the top 0.1% brightest pixels in D (farthest away pixels) as

$$A^c = \frac{1}{|P_D^{0.1\%}|} \sum_{x \in P_D^{0.1\%}} I^c(\mathbf{x}), \quad (4.2)$$

where $P_D^{0.1\%}$ is the set of positions of the top 0.1% largest-valued pixels in D .

4.2 Scene Transmission Estimation

In [7], the DCP-based transmission estimate $\tilde{t}_{rgb}(\mathbf{x}) = 1 - \min_{c, \mathbf{y} \in \Omega(\mathbf{x})} \left\{ \frac{I^c(\mathbf{y})}{A^c} \right\}$ can also be expressed as:

$$\tilde{t}_{rgb}(\mathbf{x}) = \max_{c, \mathbf{y} \in \Omega(\mathbf{x})} \left\{ 1 - \frac{I^c(\mathbf{y})}{A^c} \right\} = \max_{c, \mathbf{y} \in \Omega(\mathbf{x})} \left\{ \frac{A^c - I^c(\mathbf{y})}{A^c} \right\}. \quad (4.3)$$

The transmission is commonly written as an exponential decay term [7] based on the Beer-Lambert law [31] of light attenuation as $\tilde{t}(\mathbf{x}) = e^{-\beta d(\mathbf{x})}$, where $d(\mathbf{x}) \geq 0$ is the

	$s = 111$ $w = [.99, .42, .99]$	$s = 111$ $w = [.38, .58, .76]$	$s = 111$ $w = [.74, .7, .07]$	$s = 011$ $w = [.99, .42, .99]$	$s = 001$ $w = [.96, .89, .49]$	$s = 000$ $w = [1, .94, .87]$	$s = 000$ $w = [.31, .64, .34]$
I^c							
I_{dcp}^{rgb} [1, 4-8]							N/A
I_{dcp}^{gb} [9]	N/A		N/A				N/A
I_{dcp}^{rgb} [10]	N/A		N/A				N/A
I_{dcp}^{rgbbr} [23,24]	N/A	N/A	N/A	N/A	N/A		
D							
	(a)	(b)	(c)	(d)	(e)	(f)	(g)

Figure 4.4: Comparisons of depth estimation based on the DCP [7, 10–14], DCP variants [15, 16, 39], and the GDCP method for images with different light lighting conditions and color casts. The first row of images shows (a) A hazy image with $s = 111$, (b) an underwater image with $s = 111$, (c) a sandstorm image with $s = 111$, (d)-(f) underwater images with $s = 011, 001, 000$, and (g) a dimly lit image with $s = 000$. The next four rows show the estimated depth images using the compared methods. The last row shows the proposed depth images. Note that N/A indicates that the corresponding depth estimation method is not applicable to the image. The original image of (g) and depth images shown here undergo simple individual contrast stretching or scaling steps for display. Original images are taken from [7], [59], [58], [19], [60], and [67].

distance from the camera to the radiant object and β is the spectral volume attenuation coefficient, so $\tilde{t} \geq 0$. In [7], whenever Eq. (4.3) would yield a negative number (that is, $A^c < I^c(\mathbf{y})$, $\forall \mathbf{y} \in \Omega(\mathbf{x})$), then $\tilde{t}(\mathbf{x})$ gets clipped to zero. Therefore, scene transmission estimated using Eq. (4.3) would be inaccurate.

In order to address this problem, we propose to estimate transmission based on scene ambient light differential as:

$$\tilde{t}_{pro}(\mathbf{x}) = \max_{c, \mathbf{y} \in \Omega(\mathbf{x})} \left(\frac{|A^c - I^c(\mathbf{y})|}{\max(A^c, 1 - A^c)} \right), \quad (4.4)$$

where median filtering [9] and linearly stretching (to the range $[0.2, \max(\tilde{t}_{pro})]$) are then applied to refine the estimated transmission. The intuition behind this expression for \tilde{t}_{pro} is that the numerator captures the absolute difference between the observed intensity and the ambient light, and large values of this quantity correlate with proximity to the camera. That is, the observed intensity for a closer scene point consists more of the scene radiance and less of the ambient light, and based on Eq. (4.4), it will have large \tilde{t}_{pro} . By contrast, the observed intensity for a farther scene point consists less of the scene radiance and more of the ambient light. Therefore, its calculated \tilde{t}_{pro} is small.

4.3 DCP Generalization based on Scene Ambient Light Differential and depth-dependent color change

Our approach is a generalization of the DCP-based approaches both for ambient light estimation and transmission estimation. First, consider transmission estimation using Eq. (4.4) based on the scene ambient light differential.

1. When the ambient light is bright ($A^c \geq 0.5$) and $A^c \geq I^c$, $c \in \{r, g, b\}$, which holds for many foggy and hazy images, then $\max(A^c, 1 - A^c) = A^c$, so the expression Eq. (4.4) becomes identical to the DCP [7] as:

$$\tilde{t}_{pro}(\mathbf{x}) = \max_{c, \mathbf{y} \in \Omega(\mathbf{x})} \left(\frac{A^c - I^c(\mathbf{y})}{A^c} \right) = \tilde{t}_{rgb}(\mathbf{x}). \quad (4.5)$$

2. When the ambient light is dark ($A^c \leq 0.5$) and $A^c \leq I^c$, $c \in \{r, g, b\}$, which holds for most dimly lit images, Eq. (4.4) reduces to the DCP-based method [39] which uses

the inverted RGB channels and is meant for night videos:

$$\tilde{t}_{pro}(\mathbf{x}) = \max_{c, \mathbf{y} \in \Omega(\mathbf{x})} \left(\frac{I^c(\mathbf{y}) - A^c}{1 - A^c} \right) = \tilde{t}_{r'g'b'}(\mathbf{x}). \quad (4.6)$$

3. When $A^r \leq 0.5$ and $A^r \leq I^r$, and $A^k \geq 0.5$ and $A^k \geq I^k$, $k \in \{g, b\}$, which holds for some underwater images where red light is greatly absorbed, Eq. (4.4) reduces to the DCP-based method [16] which uses the RGB channels with the red inverted:

$$\tilde{t}_{pro}(\mathbf{x}) = \max_{\mathbf{y} \in \Omega(\mathbf{x})} \left(\frac{I^r(\mathbf{y}) - A^r}{1 - A^r}, \frac{A^g - I^g(\mathbf{y})}{A^g}, \frac{A^b - I^b(\mathbf{y})}{A^b} \right) = \tilde{t}_{r'gb}(\mathbf{x}). \quad (4.7)$$

4. In [10] and [11], Huang et al. found that sometimes images with strong color casts (in which one color channel had a small value in A^c and $I^c < A^c$) would lead to transmission over-estimation. They adopted adaptive gamma correction to try to solve the transmission over-estimation problem caused by the low observed intensity. Our general formulation has a solution to this over-estimation situation as well. For example, when $I^b \leq A^b \leq 0.5$, and $A^k \geq 0.5$ and $A^k \geq I^k$, $k \in \{r, g\}$, which holds for most sandstorm images where blue light is greatly absorbed by sand, Eq. (4.4) can be considered as a variant of \tilde{t}_{rgb} [7] which uses the RGB channels with the blue adjusted:

$$\tilde{t}_{pro}(\mathbf{x}) = \max_{\mathbf{y} \in \Omega(\mathbf{x})} \left(\frac{A^r - I^r(\mathbf{y})}{A^r}, \frac{A^g - I^g(\mathbf{y})}{A^g}, \Gamma_b \frac{A^b - I^b(\mathbf{y})}{A^b} \right), \quad (4.8)$$

where $\Gamma_b = \frac{A^b}{1 - A^b} \leq 1$ is a multiplicative factor that down weights the blue channel to overcome the over-estimation problem. That is, as A^b gets darker and $I^b \leq A^b$, Γ_b becomes smaller, making the blue channel less important in estimating transmission.

Next, ambient light estimation based on the depth-dependent color change (Eq. (4.1) and (4.2)) is a generalization of the DCP-based methods as follows:

1. D reduces to I_{dcp}^{rgb} [7] when $w_c = 1, \forall c$ and $\mathbf{s} = 111$, which means that the values in RGB channels tend to increase as depth increases. This is the situation for most hazy images and some underwater images. In such cases,

$$D(\mathbf{x}) = \min_{c, \mathbf{y} \in \Omega(\mathbf{x})} (1 - |1 - I^c(\mathbf{y})|) = \min_{c, \mathbf{y} \in \Omega(\mathbf{x})} I^c(\mathbf{y}) = I_{dcp}^{rgb}(\mathbf{x}). \quad (4.9)$$

2. D reduces to I_{dcp}^{gb} [15] when $w_r = 0, w_g = w_b = 1$ and $\mathbf{s} = -11$ (“-” in \mathbf{s} means don’t care), which means that the values in the green and blue channels tend to increase as depth increases while those in the red channel are ignored in estimating depth. This corresponds to some underwater images where red light is almost completely absorbed. In such cases,

$$D(\mathbf{x}) = \min_{\mathbf{y} \in \Omega(\mathbf{x})} \{1, 1 - |1 - I^g(\mathbf{y})|, 1 - |1 - I^b(\mathbf{y})|\} = \min_{c \in \{g, b\}, \mathbf{y} \in \Omega(\mathbf{x})} I^c(\mathbf{y}) = I_{dcp}^{gb}(\mathbf{x}). \quad (4.10)$$

3. D reduces to $I_{dcp}^{r'gb}$ [16] when $w_c = 1, \forall c$ and $\mathbf{s} = 011$, which means that the values in the green and blue channels tend to increase as depth increases while those in the red channel tend to decrease. This is the situation for most underwater images where red color attenuates more as depth increases. In such cases,

$$D(\mathbf{x}) = \min_{\mathbf{y} \in \Omega(\mathbf{x})} \{1 - I^r(\mathbf{y}), 1 - |1 - I^g(\mathbf{y})|, 1 - |1 - I^b(\mathbf{y})|\} = I_{dcp}^{r'gb}(\mathbf{x}). \quad (4.11)$$

4. D reduces to $I_{dcp}^{r'g'b'}$ [38, 39] when $w_c = 1, \forall c$ and $\mathbf{s} = 000$, which means that the values in RGB channels all tend to decrease as depth increases. This is the situation

for most images taken at night with artificial lighting. In such cases,

$$D(\mathbf{x}) = \min_{c, \mathbf{y} \in \Omega(\mathbf{x})} \{1 - I^c(\mathbf{y})\} = I'_{dcp} g' b'(\mathbf{x}). \quad (4.12)$$

4.3.1 Scene Radiance Restoration with Adaptive Color Correction

The input degraded images we are dealing with may have color casts, which need to be removed in the restoration process. In [45], the degree of a color cast is measured by $D_\sigma = \frac{\|\mu\|_2 - \|\sigma\|_2}{\|\sigma\|_2}$, where $\mu = (\mu_a, \mu_b)^T$ is a vector that contains the means of the chromatic components in the CIELab color space, and $\sigma = (\sigma_a, \sigma_b)^T$ has the chromatic variances. A larger D_σ means a stronger color cast, and $D_\sigma \leq \varepsilon$ is taken to mean no color cast, where ε is a threshold.

We found that if scene radiance is recovered from a degraded image with a color cast using Eq. (2.6), it often leads to an even stronger color cast. Thus, we propose to incorporate color correction into the IFM for removing color casts more effectively.

The approach is to adjust ambient light. Based on Eq. (2.6), we have:

$$J^c(\mathbf{x}) = \frac{I^c(\mathbf{x})}{f(\mathbf{x})} - \left[\frac{1}{f(\mathbf{x})} - 1 \right] A^c \quad (4.13)$$

where $f(\mathbf{x}) = \max(\tilde{t}_{rgb}(\mathbf{x}), t_0) \in [t_0, 1]$, and $\frac{1}{f(\mathbf{x})} - 1 \geq 0$. Hence, a large value in ambient light A^c would result in small values in J^c whereas a small value in A^c leads to an opposite result. Without considering what the “true” ambient light is, if the algorithm assumes a bright ambient light has suffused throughout the observed image, and attempts to restore the image on the basis of that assumption, the resulting restored image will be darker, as the extra brightness is removed, compared to the restoration that would have resulted from an assumption of a dimmer ambient light. A visual example can be seen in the first row of Fig. 4.5, where as the ambient light is estimated as being brighter (in terms of

luminance), the restored scene radiance gets darker.

In the same fashion, a small value in one of the color channels of the ambient light will lead to a substantial increase in that color in the restored image. The second row of Fig. 4.5 gives an example in which changing values in the red channel of A^c produces different hues of the restored images. Going from (b) to (c) to (d), the assumed values of the green and blue channels remain constant, but the red value drops from 0.65 to 0.35 to 0.05. As the ambient is assumed to have less red, the restored image based on that assumed ambient has more red. That is, we can adjust the estimate of ambient light based on the input image in order to remove color casts.




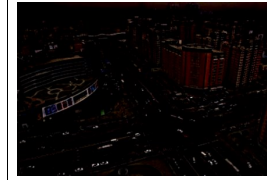

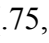
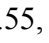
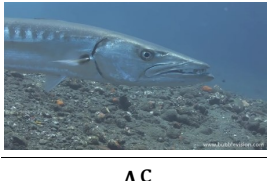
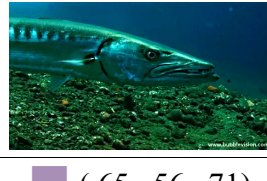



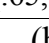
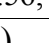
			
A^c	 (.65, .56, .71)	 (.35, .56, .71)	 (.05, .56, .71)
			
A^c	 (.75, .55, .37)	 (.82, .69, .55)	 (1, .88, .70)
(a)	(b)	(c)	(d)

Figure 4.5: Examples of changing hue or brightness of restored scene radiance by adjusting ambient light with given transmission estimated using the GDCP method. (a) Original images. (b), (c), and (d) are the restored images using different ambient light. The original images are from [10] and [59].

Iqbal et al. [44] proposed to keep constant the color channel with the dominant color cast, and scale up the other channels to correct the image color based on the gray world assumption [46]. This approach may suffer from color distortion when there is a strong color cast. Motivated by [44, 45], and using D_σ as defined in [45], we calculate color correction coefficients φ^c as

$$\varphi^c = \left\{ \frac{\max_{k \in \{r, g, b\}} I_{avg}^k}{I_{avg}^c} \right\}^{\frac{1}{\sqrt{\max(\xi(D_\sigma), 1)}}}, \xi(z) = \begin{cases} z, & z > \varepsilon \\ \infty, & z \leq \varepsilon, \end{cases} \quad (4.14)$$

where $I_{avg}^c = \max(\mathbf{avg}_x I^c(\mathbf{x}), 0.1)$, and $\frac{1}{\sqrt{\max(\xi(D_\sigma), 1)}}$ aims to avoid color distortion when there is a strong color cast. Here, we set $\varepsilon = 0$.

Then, we adjust the ambient light A^c with the color correction coefficients φ^c as $A_\varphi^c = \frac{A^c}{\varphi^c}$. At the end, by putting A_φ^c into Eq. (2.6), the resulting estimate of scene radiance is

$$J_\varphi^c(\mathbf{x}) = \frac{I^c(\mathbf{x}) - A_\varphi^c}{\max(\tilde{t}_{pro}(\mathbf{x}), t_0)} + A_\varphi^c, \quad (4.15)$$

where t_0 is set to 0.3 for the GDCP method. According to Eq. (4.14), when $D_\sigma \leq \varepsilon$, which means there is no color cast, then $\varphi^c = 1$, and $A_\varphi^c = A^c$. Otherwise, we use $\frac{1}{\sqrt{\max(D_\sigma, 1)}}$ to adjust the color correction coefficients. Fig. 4.6 shows examples of scene radiance restoration with and without incorporating adaptive color correction coefficients. We can see that the restored images without using correction coefficients have stronger color casts than the original images while the ones using correction coefficients present more visually pleasing results. Therefore, instead of performing color correction on the recovered J , we can achieve both scene radiance restoration and color correction by adjusting the ambient light estimate with the color correction coefficients.

4.4 Experimental Results

In this section, we evaluate various kinds of DCP-based restoration methods for foggy, hazy, sandstorm, and underwater images. For terrestrial images, we compare the GDCP method against several state-of-the-art IFM-based image restoration methods described in [7, 10, 11, 21, 23]. For the underwater images, we choose the methods

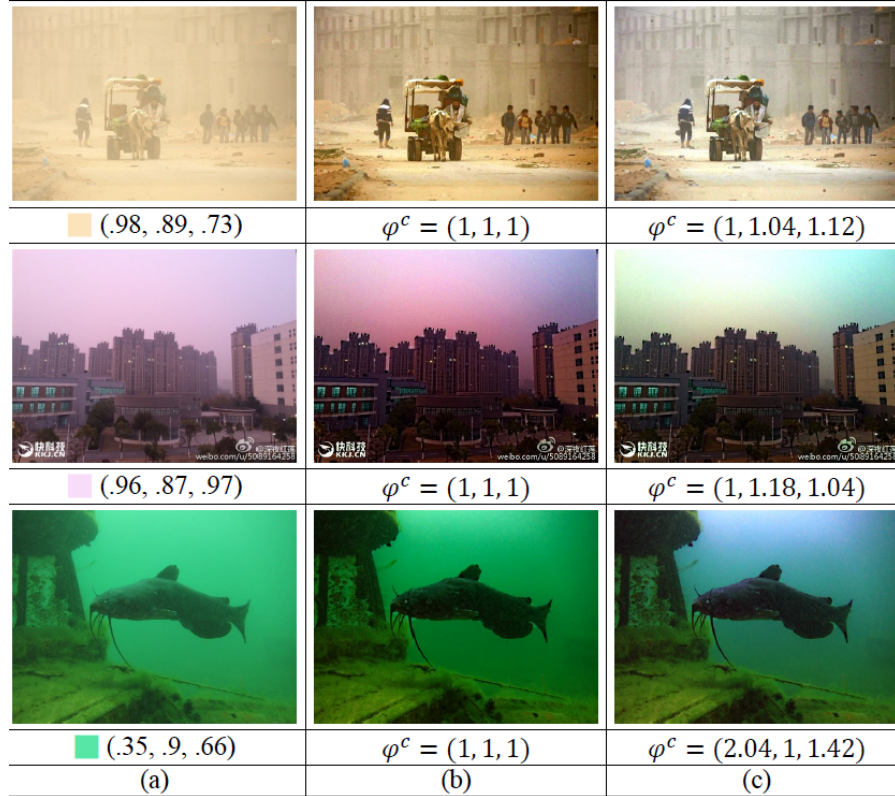


Figure 4.6: Examples of scene radiance restoration with and without adaptive color correction. (a) Original images with the estimated ambient light. Restored scene radiance (b) without, and (c) with using color correction coefficients. The original images are from [11], kkj.cn, and [62].

described in [15, 17–19] to compare with our proposed one. The output images are evaluated in two ways:

1. Subjective visual comparison including examination of estimated transmission;
2. Objective quantitative no-reference quality assessment of restored images.

4.4.1 Qualitative Assessment

In the visual comparison, we use 10 degraded images, including 2 hazy/foggy, 4 sandstorm, and 4 underwater images, with different color tones and lighting conditions for testing.

In Fig. 4.7, the original image is hazy with bright ambient light and does not have a color cast. All methods work well for this case.

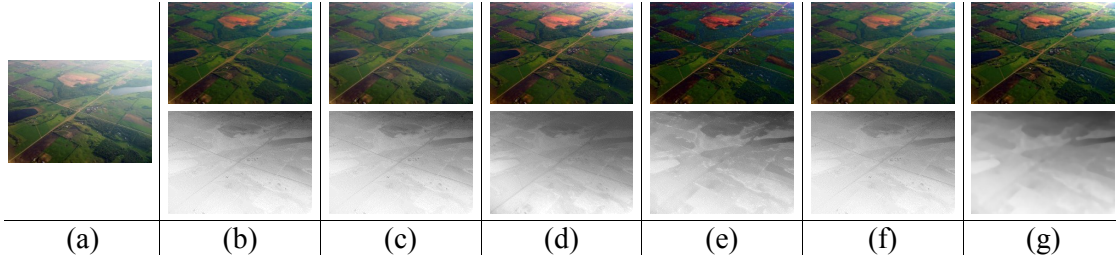


Figure 4.7: A restoration example where all methods are successful. (a) The original image. The restored results, and the corresponding transmission maps obtained using: (b) [7], (c) [21], (d) [23], (e) [10], (f) [11], and (g) the GDCP method. The original image is from [6].

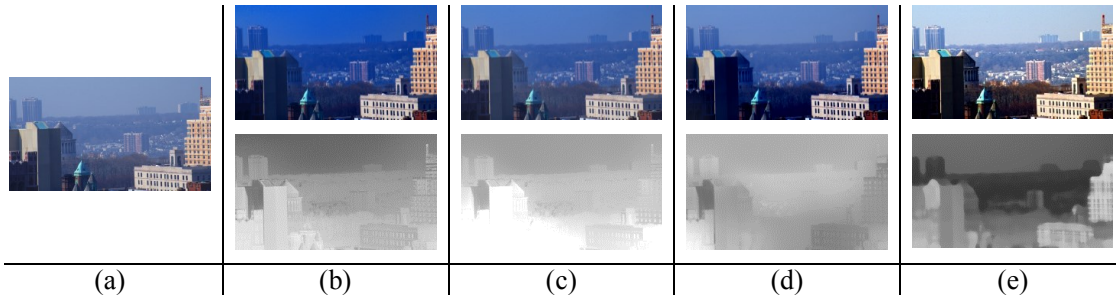


Figure 4.8: An example of restoring a dark hazy image with a color cast. (a) The original image. The restored results, and the corresponding transmission maps obtained using: (b) [7], (c) [21], (d) [23], and (e) the GDCP method without considering color correction ($\varphi^c = 1$). The original image is from [6].

Fig. 4.8 gives an example of restoring a dark hazy image with a bluish color cast using restoration methods without color correction. So, in this example, we set $\varphi^c = 1, \forall c \in \{r, g, b\}$ for the GDCP method, resulting in $A_\varphi^c = A^c$. In the figure, the methods [7, 21, 23] barely enhance the contrast of the image because of imprecise transmission estimation for dark hazy images, while the processed result using the GDCP method has better contrast due to a more accurate transmission map estimation. Fig. 4.9 demonstrates more restoration results for the dark hazy image in Fig. 4.8(a) but using

methods with color correction explicitly incorporated into the algorithm. As can be seen, the image obtained using [10] presents even a more serious color cast. The method [11] estimates transmission inaccurately, wrongly regarding the entire scene as very close to the camera, leading to a negligible restoration result. The GDCP method, adjusting ambient light using color correction coefficients $\varphi^c = [1.44, 1.28, 1]$, is able to remove the color cast by magnifying intensities in the red and green channels while enhancing the contrast for the input image.

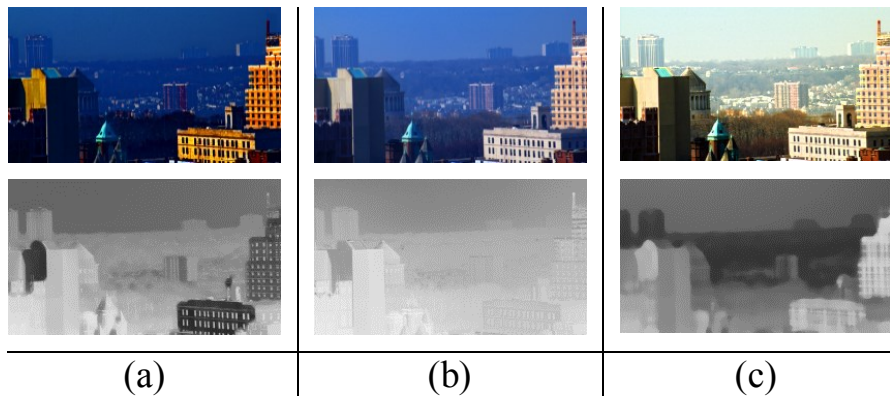


Figure 4.9: Restoring the dark hazy image with a color cast in Fig. 4.8 (a) using the methods with color correction incorporated. The restored results, and the corresponding transmission maps obtained using: (a) [10], (b) [11], (c) the GDCP method ($\varphi^c = [1.44, 1.28, 1]$).

Fig. 4.10 shows four examples of restoring sandstorm images with different color distributions. Based on the histograms of the original images, we can consider the images from the first to last row to be shot in sandstorms of different densities ranging from thin to thick. In the first row of Fig. 4.10, the scene transmission estimated by [11], [21], and [23] is inaccurate, so their processed images are not sufficiently enhanced. Although the processed image by the method [7] has good contrast compared to the original image, it has a more severe color cast. The processed images by the GDCP method and [10] both look color corrected, but the one using the GDCP method has better contrast.

For the second image, the transmission estimated using the methods [21, 23] is

wrong, and the restored images are almost the same as the original sandstorm image. The DCP method [7] only enhances contrast of the image but does not deal with the color cast. The method [11] fails to enhance contrast of the image and does poorly on color correction. The GDCP method and [10] both correct color for the image while the restored image using the GDCP method has better contrast.

For the third image, the processed images obtained using the method [7,10,11,21] are hardly enhanced. The method [11] does not correct color properly, so the result image looks a little greenish. Although the method [23] enhances contrast of the image, its color cast problem worsens as well. The GDCP method is able to produce a better enhanced and color-corrected result.

For the last image, the original image with a thick sandstorm has very little blue color, which invalidates all the methods except for the proposed GDCP method. Lastly, Fig. 4.11 demonstrates restoration of underwater images with different color tones and lighting conditions. The first row of Fig. 4.11 shows an example of restoring a bluish underwater image. All methods work well for this case, and the result images all look restored and enhanced although some color differences exist.

The second original image of Fig. 4.11 is dimly lit, which invalidates the DCP-, MIP-, and MILP-based methods. Therefore, the processed images by the DCP-based [15, 17], MIP-based [19], and MILP-based [18] methods look insignificantly restored because of the incorrect transmission estimation. The GDCP method based on scene ambient light differential can estimate scene transmission more accurately and generate a more satisfying enhanced result for the image.

The third input image of Fig. 4.11 shows an example of restoring an image that has more blue and green color than red. We can see that the processed images from the methods [15,17,19] are negligibly restored because of inaccurate transmission estimation. The method [18] can slightly enhance the contrast of this image, but the processed image

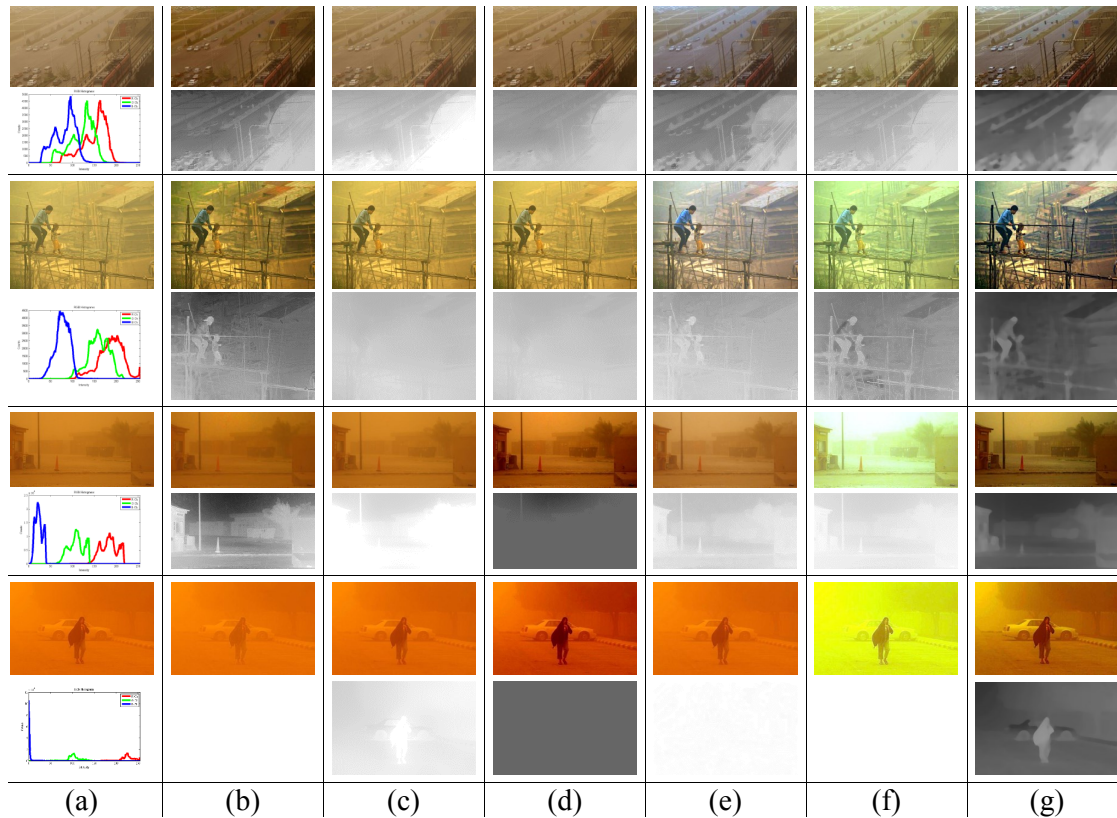


Figure 4.10: Example of restoring sandstorm images with different color distributions. (a) The original images and their color histograms. The restored results, and the corresponding transmission maps obtained using: (b) [7], (c) [21], (d) [23], (e) [10], (f) [11], and (g) the GDCP method. The original images are from [10], [64], and [65]. Note that it is better to view this figure on a screen.

by the proposed method is more vivid and has better contrast.

The last image of Fig. 4.11 shows an example of restoring a greenish image, where the methods [15, 17–19] barely restore the image, whereas the GDCP method produces a more visually pleasing result with better contrast.

4.4.2 Quantitative Assessment

Image restoration methods can also involve objective evaluation [25, 27, 28, 30]. For terrestrial scenes, we choose 58 terrestrial images with haze, fog, and sandstorm,

etc., shown in Fig. 4.12, and adopt three non-reference image quality metrics for testing. The first two are blind contrast metrics that measure gradient ratios at visible edges [30], where one is the metric e that calculates an edge restoration rate and the other is the metric r that assesses quality of contrast restoration. Large values for e and r mean better contrast. The third one is the Natural Image Quality Evaluator (NIQE) [25], a blind image quality assessment model that measures the quality of distorted images based on the space domain natural scene statistics, where a small value represents better quality. Table 4.1 shows the average e , \bar{r} and NIQE values for the restored images from all the compared methods of Fig. 4.12, where the proposed method performs better than the other methods.

For underwater scenes, we choose 55 underwater images with different color tones and lighting conditions, shown in Fig. 4.13, and adopt three non-reference image quality metrics for testing: UIQM [27], UCIQE [28], and NIQE. Table 4.2 demonstrates average UIQM, UCIQE, and NIQE values of the original images in Fig. 4.13 and their restored versions from all the compared methods, where the GDCP method outperforms the other methods.

Table 4.1: Average e , \bar{r} and NIQE values for the restored images from all the compared methods of Fig. 4.12.

	Original	[7]	[21]	[23]	[10]	[11]	Proposed
e	–	0.72	0.12	0.60	0.55	0.29	1.54
\bar{r}	–	1.35	1.12	1.44	1.35	1.42	2.12
NIQE	4.46	4.13	4.57	4.23	4.22	4.18	3.64

4.5 Acknowledgement

This chapter, in full, is a reprint of a published paper, Y.-T. Peng and P. C. Cosman, “Single Image Restoration using Scene Ambient Light Differential,” *IEEE Int. Conf. on*

Table 4.2: Average UIQM, UCIQE, and NIQE values of the original images in Fig. 4.13 and their restored versions from all the compared methods.

	Original	[19]	[15]	[17]	[18]	Proposed
UIQM	2.82	3.55	3.65	3.55	3.61	4.16
UCIQE	0.51	0.57	0.59	0.57	0.55	0.63
NIQE	4.94	4.17	4.07	4.15	4.12	3.85

Imag. Process. (ICIP), pp. 1953-1957, Sep. 2016, and of a submitted paper, Y.-T. Peng, K. Cao, and P. C. Cosman, “Generalization of the Dark Channel Prior for Single Image Restoration” (submitted to *IEEE Trans. Image Process.*, Jul. 2017). The dissertation author was the primary investigator and author of these papers.

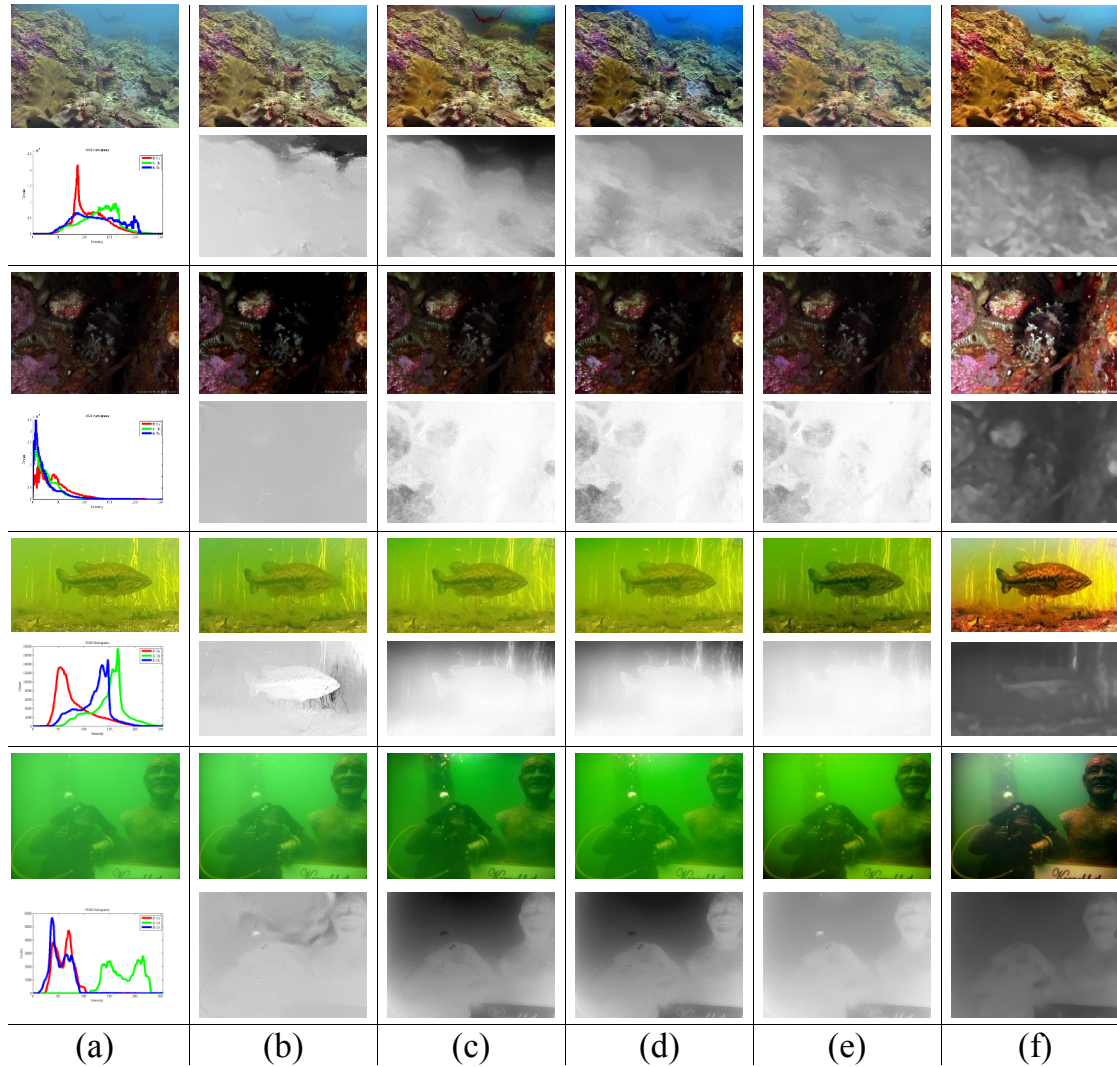


Figure 4.11: Example of restoring an underwater images with different color tones and lighting conditions. (a) The original images. The restored results, and the corresponding transmission maps obtained using: (b) [19], (c) [15], (d) [17], (e) [18], (f) the GDCP method. The original images come from [59], and [16]. Note that it is better to view this figure on a screen.

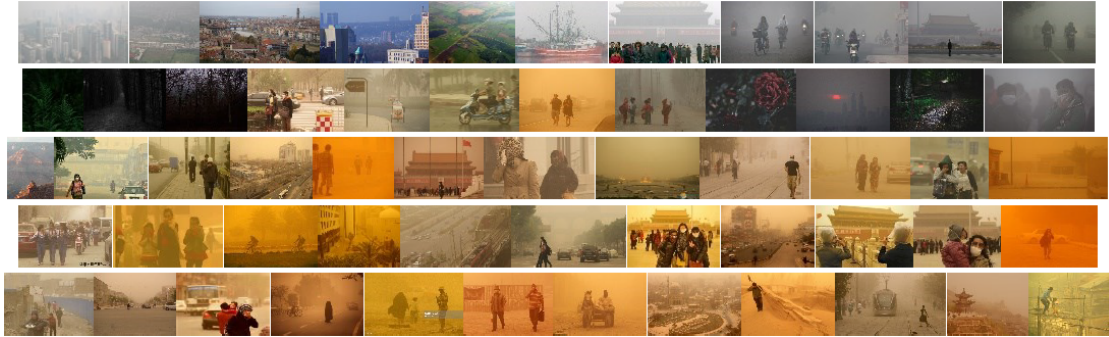


Figure 4.12: Terrestrial images for quantitative testing. The images are from [6,7,10,11], and Google Images.

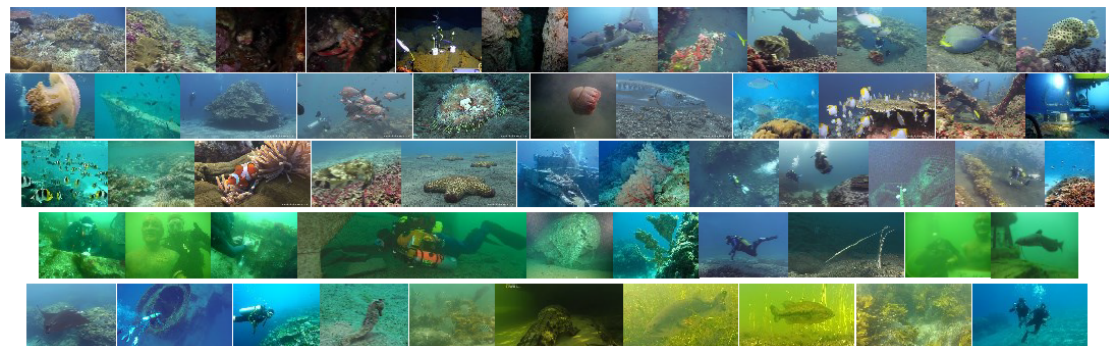


Figure 4.13: Underwater images for quantitative testing. The images are from [16, 19, 59], and Google Images.

Chapter 5

Conclusion and Future Work

For underwater image restoration, we have proposed to exploit image blurriness and light absorption to estimate the background light, scene depth, and transmission maps for underwater scenes with different color tones and lighting conditions instead of using the DCPs or MIP, which only work for limited cases. Satisfying restored and enhanced results were demonstrated. The proposed depth estimation works well for a wide variety of underwater images.

For images degraded by light scattering and absorption, such as hazy, sandstorm, underwater images, and dimly-lit images, we proposed to use the depth-dependent color change, scene ambient light differential, and adaptive color-corrected IFM to better restore them. We first analyze the depth-dependent color change of the input image to measure scene depth for ambient light estimation. With the estimate of ambient light, the scene ambient light differential is calculated to estimate scene transmission. Lastly, the input image is restored based on the adaptive color-corrected IFM. This unifying framework was demonstrated to work for a wide variety of degraded images with different color tones/casts, contents, and lighting conditions

There are several possible future directions to extend our work as follows.

1. To extend image restoration to video restoration, instead of directly applying an image restoration approach to each frame of a video, we may use temporal redundancy between frames to reduce computation costs. If an IFM-based restoration approach is adopted, ambient light should be unchanged if the lighting condition remains the same. Thus, it is unnecessary to estimate it for each frame. Transmission for the background should also tend to change only slightly from frame to frame.
2. Even though the proposed generalized DCP works for a wide variety of different degraded images, it will still fail for a scene that violates the underlying assumptions of the DCP. For example, suppose a white object exists in a close scene of a hazy image where red, green, and blue lights increase as the depth increases. Based on the DCP, the object will be wrongly regarded as being far. To resolve this problem, we may combine image blurriness with the DCP to increase accuracy of depth estimation.

Bibliography

- [1] C. Ancuti, C. O. Ancuti, T. Haber, and P. Bekaert, "Enhancing underwater images and videos by fusion," in *Proc. IEEE Conf. Comput. Vis. Pattern Recognit. (CVPR)*, pp. 81-88, June 2012.
- [2] C. O. Ancuti and C. Ancuti, "Single image dehazing by multi-scale fusion," *IEEE Trans. Image Process.*, vol. 22, no. 8, pp. 3271-3282, Aug. 2013.
- [3] S. Q Duntley "Light in the sea." *J. Opt. Soc. Amer.*, vol. 53, no. 2, pp. 214233, 1963.
- [4] S. G. Narasimhan and S. K. Nayar, "Chromatic Framework for Vision in Bad Weather," in *Proc. IEEE Conf. Comput. Vis. Pattern Recognit. (CVPR)*, vol. 1, pp. 598-605, June 2000.
- [5] S. G. Narasimhan and S. K. Nayar, "Vision and the Atmosphere," *Int. J. Comput. Vis.*, vol. 48, pp. 233-254, 2002.
- [6] R. Fattal, "Single image dehazing," *ACM Trans. Graphics*, vol.27, no. 3, pp. 721-729, 2008.
- [7] K. He, J. Sun, and X. Tang, "Single image haze removal using dark channel prior," *IEEE Trans. Pattern Anal. Mach. Intell.*, vol. 33, no. 12, pp. 2341-2353, Dec. 2011.
- [8] H. Xu, J. Guo, Q. Liu, and L. Ye, "Fast image dehazing using improved dark channel prior," in *Proc. IEEE Int. Conf. Inf. Sci. Technol.*, Mar. 2012, pp. 663-667.
- [9] K. B. Gibson, D. T. Vo, and T. Q. Nguyen, "An investigation of dehazing effects on image and video coding," *IEEE Trans. Image Process.*, vol. 21, no. 2, pp. 662-673, Feb. 2012.
- [10] S.-C. Huang, B.-H. Chen, and W.-J. Wang, "Visibility restoration of single hazy images captured in real-world weather conditions," *IEEE Trans. Circuits Syst. Video Technol.*, vol. 24, no. 10, pp. 1814-1824, Oct. 2014.
- [11] S.-C. Huang, J.-H. Ye, and B.-H. Chen, "An Advanced Single-Image Visibility Restoration Algorithm for Real-World Hazy Scenes," *IEEE Trans. Ind. Electron.*, vol. 62, no. 5, pp. 2962-2972, May. 2015.

- [12] L. Chao and M. Wang, "Removal of water scattering," in *Proc. IEEE Int. Conf. Comput. Eng. and Technol. (ICCET)*, vol. 2, pp. 35-39, Apr. 2010.
- [13] H. Yang, P. Chen, C. Huang, Y. Zhuang and Y. Shiao, "Low complexity underwater image enhancement based on dark channel prior," *Int. Conf. Innov. in Bio-inspired Comput. and App. (IBICA)*, pp. 17-20, Dec. 2011. 17-20, 2011.
- [14] J. Y. Chiang and Y.-C. Chen, "Underwater image enhancement by wavelength compensation and dehazing," *IEEE Trans. Image Process.*, vol. 21, pp. 1756-1769, Apr. 2012.
- [15] P. Drews, E. do Nascimento, F. Moraes, S. Botelho, and M. Campos, "Transmission Estimation in Underwater Single Images," in *Proc. IEEE Int. Conf. Comput. Vis. Workshops (ICCVW)*, pp. 825-830, Dec. 2013.
- [16] A. Galdran, D. Pardo, A. Picn, and A. Alvarez-Gila, "Automatic Red-Channel underwater image restoration," *J. of Vis. Comm. and Imag. Repres.*, vol. 26, pp. 132-145, Jan. 2015.
- [17] X. Zhao, J. Tao, and Q. Song. "Deriving inherent optical properties from background color and underwater image enhancement," *Ocean Eng.*, vol. 94, pp. 163-172, Jan. 2015.
- [18] C. Li, J. Guo, S. Chen, Y. Tang, Y. Pang, and J. Wang, "Underwater image restoration based on minimum information loss principle and optical properties of underwater imaging," *IEEE Int. Conf. on Imag. Process. (ICIP)*, pp. 1993-1997, Sep. 2016.
- [19] N. Carlevaris-Bianco, A. Mohan, and R. M. Eustice, "Initial results in underwater single image dehazing," in *Proc. IEEE Oceans*, pp. 1-8, Sep. 2010.
- [20] https://en.wikipedia.org/wiki/Colour_cast
- [21] Q. Zhu, J. Mai, and L. Shao, "A Fast Single Image Haze Removal Algorithm Using Color Attenuation Prior," *IEEE Trans. Image Process.*, vol. 24, no. 11, pp. 3522-3533, Nov. 2015.
- [22] B. Cai , X. Xu, K. Jia, C. Qing, and D. Tao, "DehazeNet: An End-to-End System for Single Image Haze Removal," *IEEE Trans. Image Process.*, vol. 25, no. 11, pp. 5187-5198, Nov. 2016.
- [23] X. Fan, Y. Wang, X. Tang, R. Gao, and Z. Luo, "Two-Layer Gaussian Process Regression with Example Selection for Image Dehazing," *IEEE Trans. Circuits Syst. Video Technol.*, 2016 (accepted).
- [24] A. Mittal, A. K. Moorthy, and A. C. Bovik, "No-Reference Image Quality Assessment in the Spatial Domain," *IEEE Trans. Image Process.*, vol. 21, no. 12, pp. 4695-4708, Dec. 2012.

- [25] A. Mittal, R. Soundararajan, and A. C. Bovik, "Making a "Completely Blind" image quality analyzer," *IEEE Signal Process. Lett.*, vol. 20, no. 3, pp. 209-212, Mar. 2013.
- [26] K. B. Gibson and T. Q. Nguyen, "A No-Reference Perceptual Based Contrast Enhancement Metric for Ocean Scenes in Fog," *IEEE Trans. Image Process.*, vol. 22, no. 10, pp. 3982-3993, Jun. 2013.
- [27] K. Panetta, C. Gao, and S. Agaian, "Human-Visual-System-Inspired Underwater Image Quality Measures," *IEEE J. of Ocean. Eng.*, pp. 1-11, 2015.
- [28] M. Yang and A. Sowmya, "An Underwater Color Image Quality Evaluation Metric," *IEEE Trans. Image Process.*, vol. 24, no. 12, pp. 6062-6071, Dec. 2015.
- [29] Z. Wang, A. C. Bovik, H. R. Sheikh and E. P. Simoncelli, "Image quality assessment: From error visibility to structural similarity," *IEEE Trans. Image Process.*, vol. 13, no. 4, pp. 600-612, Apr. 2004.
- [30] N. Hautière, J.-P. Tarel, D. Aubert, and E. Dumon, "Blind contrast enhancement assessment by gradient ratioing at visible edges," *Image Analysis & Stereology Journal*, vol. 27, no. 2, pp. 87-95, Jun. 2008.
- [31] P. Bouguer, "Essai d'Optique, sur la gradation de la lumiere," Claude Jombert, 1729.
- [32] A. Levin, D. Lischinski, and Y. Weiss, "A Closed-Form Solution to Natural Image Matting," *IEEE Trans. Pattern Anal. Mach. Intell.*, vol. 30, no. 2, pp. 228 - 242, Feb. 2008.
- [33] K. He, J. Sun, and X. Tang, "Guided image filtering," *IEEE Trans. Pattern Anal. Mach. Intell.*, vol. 35, no. 6, pp. 1397-1409, Oct. 2012.
- [34] H. Wen, Y. Tian, T. Huang, and W. Gao, "Single underwater image enhancement with a new optical model," in *Proc. IEEE Int. Symp. Circuits & Syst. (ISCAS)*, May 2013, pp. 753-756.
- [35] S. Emberton, L. Chittka, and A. Cavallaro, "Hierarchical rank-based veiling light estimation for underwater dehazing," *British Machine Vision Association*, pages 125.1-125.12, 2015.
- [36] Y.-T. Peng, X. Zhao, and P. C. Cosman, "Single Underwater Image Enhancement using Depth Estimation based on Blurriness," in *Proc. IEEE Int. Conf. on Imag. Process. (ICIP)*, pp. 4952-4956, Sep. 2015.
- [37] Y.-T. Peng and P. C. Cosman, "Single Image Restoration using Scene Ambient Light Differential," *IEEE Int. Conf. on Imag. Process. (ICIP)*, pp. 1953-1957, Sep. 2016.

- [38] X. Jiang, H. Yao, S. Zhang, X. Lu, and W. Zeng, "Night video enhancement using improved dark channel prior," *IEEE Int. Conf. on Imag. Process. (ICIP)*, pp. 553-557, Sep. 2013.
- [39] X. Dong and J. Wen, "Low lighting image enhancement using local maximum color value prior," *J. Front. Comput. Sci.*, vol. 10, no. 1, pp. 147-156, Nov. 2015.
- [40] Q. Li and Z. Wang, "Reduced-reference image quality assessment using divisive normalization-based image representation," *IEEE J. Sel. Topics Signal Process.*, vol. 3, no. 2, pp. 202-211, Apr. 2009.
- [41] R. Soundararajan and A. C. Bovik, "RRED indices: Reduced reference entropic differencing for image quality assessment," *IEEE Trans. Image Process.*, vol. 21, no. 2, pp. 517-526, Feb. 2011.
- [42] P. Soille, "Morphological Image Analysis: Principles and Applications," Springer-Verlag, 1999, pp. 173-174.
- [43] Y. Y. Schechner and N. Karpel, "Recovery of Underwater Visibility and Structure by Polarization Analysis," *IEEE J. of Ocean. Eng.*, vol. 30, no. 3, pp. 570-587, July 2005.
- [44] K. Iqbal, M. Odetayo, A. James, R. A. Salam and A. Z. H. Talib, "Enhancing the Low Quality Images using Unsupervised Color Correction Method," in Proc. IEEE Int. Conf. on Syst., Man, Cybern., 2010, pp. 1703-1709.
- [45] F. Gasparini and R. Schettini, "Color correction for digital photographs," in Proc. *IEEE Int. Conf. Image Anal. Process.*, Sep. 2003, pp. 645-651.
- [46] A. C. Hurlbert, "Formal connections between lightness algorithms," *J. Opt. Soc. Amer. A*, vol. 3, no. 10, pp. 1684-1693, 1986.
- [47] D. Lowe, "Distinctive image features from scale-invariant keypoints," *Int. Journal of Comp. Vision. IEEE*, 2004.
- [48] B. L. McGlamery, "A computer model for underwater camera system," in Proc. *SPIE*, vol. 208, pp. 221231, 1979.
- [49] K. J. Voss, "Simple empirical model of the oceanic point spread function," *Appl. Opt.*, vol. 30, no. 18, pp. 2647-2651, 1991.
- [50] C. D. Mobley, *Radiative Transfer in the Ocean*. Encyclopedia of ocean sciences, pp. 2321-2330, 2001.
- [51] W. S. Jagger and W. R. A. Muntz, "Aquatic vision and the modulation transfer properties of unlighted and diffusely lighted natural waters," *Vis. Res.*, vol. 33, no. 13, pp. 1755-1763, 1993.

- [52] N. G. Jerlov, *Optical Oceanography*. Amsterdam, The Netherlands: Elsevier, 1968.
- [53] R. Fattal, "Dehazing using color-lines," *ACM Trans. Graphics*, vol.28, no. 4, 2014
- [54] http://live.ece.utexas.edu/research/quality/BRISQUE_release.zip
- [55] R. A. Hummel, "Image enhancement by histogram transformation," *Computer Graphics and Image Processing*, vol.6, no.2, pp.184-195, 1977.
- [56] K. Zuiderveld, "Contrast Limited Adaptive Histogram Equalization," *Graphic Gems IV*. San Diego: Academic Press Professional, pp. 474-485, 1994.
- [57] http://en.wikipedia.org/wiki/Pisces_V
- [58] <https://www.cnn.com>
- [59] <https://www.bubblevision.com>
- [60] <https://reeflifesurvey.com>
- [61] <http://amazingpict.com/hd-wallpapers-background-images/>
- [62] <https://www.youtube.com/watch?v=g9DQvW3aDgg>
- [63] <https://www.wsj.com>
- [64] <http://johnsonmatel.com/>
- [65] <http://blog.asiantown.net/>
- [66] <http://www.scout.com/>
- [67] <https://www.pinterest.com/>
- [68] <https://www.soest.hawaii.edu/HURL>